coatings

MDPI

Article

Surface Roughness-Dependent Morphology and Corrosion Protection of Polymeric–Ceramic ZnO Nanocoatings on Ti6Al4V Alloys

Şakir Altınsoy [1,*], Nuray Beköz Üllen [2,*], Gizem Karabulut Şevk [2] and Selcan Karakuş [3,4]

[1] Department of Biomedical Engineering, Faculty of Engineering and Architecture, Istanbul Yeni Yuzyil University, Istanbul 34010, Turkey
[2] Department of Metallurgical and Materials Engineering, Faculty of Engineering, Istanbul University-Cerrahpaşa, Istanbul 34200, Turkey; gizem.karabulut@iuc.edu.tr
[3] Department of Chemistry, Faculty of Engineering, Istanbul University-Cerrahpaşa, Istanbul 34200, Turkey; selcan@iuc.edu.tr
[4] Health Biotechnology Joint Research and Application Center of Excellence, Esenler, Istanbul 34220, Turkey
* Correspondence: sakir.altinsoy@yeniyuzyil.edu.tr (Ş.A.); nbekoz@iuc.edu.tr (N.B.Ü.)

Highlights

- Xanthan gum–celite organic matrix blend-mediated ZnO NPs were synthesized using an ultrasonication process.
- The surface roughness of Ti6Al4V alloys was changed by turning processes at different feed rates.
- The roughened surface of Ti6Al4V alloys was coated with spherical-shaped ZnO NPs.
- Organic–inorganic nanostructures were homogeneously distributed with good dispersion on the substrate surface.
- After coating, protection effectiveness of up to 98.48% was achieved.

Abstract

The release of aluminum (Al) and vanadium (V) ions represents a critical concern limiting the long-term performance and biocompatibility of Ti6Al4V-based permanent orthopedic implants. This study focuses on improving the corrosion resistance of Ti6Al4V alloys through the application of a novel organic–inorganic ZnO nanocoating. In addition, the present study investigated the influence of substrate roughness on surface morphology, microhardness, and wettability characteristics. Xanthan gum (XG) and celite (CE) were utilized as a biopolymeric–ceramic matrix for the ceramic–biopolymer-assisted synthesis of ZnO nanoparticles (ZnO NPs) through ultrasonication, which was subsequently followed by deposition onto Ti6Al4V substrates with varying surface roughness (Ra) achieved through controlled turning. The synthesized XG/CE-ZnO NPs exhibited a uniform spherical morphology with an average particle size of nearly 50 nm and a hexagonal wurtzite crystalline structure, as confirmed by TEM, XRD, and FTIR analyses. Contact angle (CA) measurements indicated that wettability increased with higher Ra, while SEM with energy-dispersive X-ray spectroscopy characterization revealed morphology transitions from smooth, homogeneous coatings to agglomerate, star-like nanostructures as Ra increased. Electrochemical testing in Ringer's solution demonstrated a significant improvement in corrosion resistance after coating, with protection efficiencies ranging from 95.18% to 98.48%, particularly for smoother substrates. Although increased Ra may enhance coating adhesion through mechanical interlocking, smoother substrates promote the formation of more homogeneous coatings, resulting in superior corrosion protection. These results demonstrate the significant influence of substrate topography in enhancing the functional performance

Check for updates

Academic Editor: Min Zhang

Received: 12 June 2026
Revised: 6 July 2026
Accepted: 8 July 2026
Published: 11 July 2026

Copyright: © 2026 by the authors. Licensee MDPI, Basel, Switzerland. This article is an open access article distributed under the terms and conditions of the Creative Commons Attribution (CC BY) license.

of biocompatible ZnO nanocoatings, providing valuable insights for the surface engineering of metallic implants.

Keywords: organic–inorganic nanocoatings; ZnO nanoparticles; surface roughness; Ti6Al4V alloy; corrosion resistance; wettability

1. Introduction

Ti6Al4V alloy is commonly used as a material for metallic implants and prostheses in orthopedics, dentistry, and other medical fields due to its remarkable corrosion resistance, excellent mechanical properties, bone-like elasticity modulus, low density, and minimal potential for allergic reactions. Additionally, it is non-magnetic, has a low risk of chemical interaction with injected materials, and offers excellent biocompatibility for long-term implantation [1]. However, metal-based implants can suffer from surface degradation due to interactions with bodily fluids and organs, leading to issues such as corrosion, wear, and fatigue. The ion release of aluminum (Al) and vanadium (V) is a crucial concern that affects the service life of biomedical devices and implants made from Ti6Al4V. This is a significant concern because these ions have been associated with cytotoxic effects, inflammatory responses, and impaired osseointegration, which may compromise the long-term performance of orthopedic and dental implants. The surface properties of metal-based implants are critical to their performance, reliability, and lifespan. Both the intrinsic physical characteristics of the material and the integrity of the implant's outer surface influence these properties. The surface integrity, wettability, and functionalization for antibacterial and anticorrosive effects can be adjusted and optimized to provide a multifunctional performance [2].

Enhancing the surface and anticorrosion performance of titanium-based materials is an important area of scientific research [3]. One prominent approach is implant surface coating with various metal-based NPs to improve surface properties, functionality, and protection [4–8]. These nanostructures exhibit unique features not found in larger-scale systems, enabling them to perform a range of novel functions across multiple domains. As a result, they have found extensive applications in the materials science, electronics, healthcare, and energy sectors [9]. Nanostructure-based coatings are ultra-thin layers that are applied to surfaces by assembling NPs. These coatings can significantly enhance or protect the surface properties of substrate materials by providing characteristics such as durability, corrosion resistance, and antibacterial features [10,11]. Their unique properties and versatility have attracted considerable attention across diverse fields, from electronics to biomedical applications. Additionally, several studies have reported a reduced corrosion potential for surfaces treated with nanocoatings compared to their uncoated base metal counterparts [12].

Coatings made from silver (Ag) [12,13], copper oxide (CuO) [10,14], gold (Au) NPs [15], and titanium dioxide (TiO_2) [16] have been extensively studied in the literature. Among these NPs, zinc oxide (ZnO) stands out as a promising option due to its excellent semiconducting, piezoelectric, and photocatalytic properties [17–24]. The integrity of the coating's surface is crucial for defining its performance characteristics, which include adhesion strength, optical properties, and catalytic activity. In addition to Ra, other key structural aspects of surface integrity—such as surface topography, microstructure, and microhardness—also significantly affect the multifunctional performance of metallic bio-implants [25]. Surface modifications have become increasingly popular in implant applications, providing effective solutions to enhance the biocompatibility and functionality of implants [26].

Research indicates that an implant's mechanical characteristics, design, compatibility, and load transmission are all greatly influenced by its surface integrity. Surface characteristics play a vital role in the healing of bone tissue; Ti and its alloys are highly reactive, influencing the growth of germs [27].

Surface integrity plays a crucial role in and is closely related to biocompatibility. A key factor in the success of implantation is the interaction among mechanical characteristics, macro-microstructure, surface integrity, and roughness [28,29]. Many studies have highlighted the critical role of Ra in cell adhesion and proliferation, emphasizing the need to optimize Ra for desired outcomes. To enhance both surface and corrosion characteristics of the Ti6Al4V alloy, this study employed various surface treatments, including machining and nanocoating, to create multifunctional surfaces [30–32].

In this study, novel XG/CE-ZnO NPs were synthesized and coated on Ti6Al4V alloy with varying Ra values, and superficial and microstructural characterizations were performed. ZnO-based NPs were synthesized in an XG/CE blend matrix using the ultrasonication method and coated onto Ti6Al4V parts via the drop-casting method. XG is a biopolymeric material composed of an anionic polysaccharide structure. Its unique properties make it suitable for drug delivery systems. When combined with guar or locust bean gum, XG forms flexible gels and stabilizes drug suspensions in aqueous solutions [33]. CE, commonly known as diatomite, diatomaceous earth, or infusorial earth, is primarily composed of SiO_2. As an inert biosupport material, CE possesses an internal cavity surrounded by an interconnected porous silica framework containing SiO_2 and various inorganic oxides, which facilitates efficient physical adsorption. CE is generally used in various applications, such as fillers, filter aids, heat-insulating material, and clarifying agents [34]. The combined use of XG and CE was selected to exploit the complementary advantages of both materials. XG acts as a natural biopolymer that stabilizes ZnO NPs by reducing agglomeration and improving their dispersion during synthesis, whereas CE serves as an inorganic support with a high surface area, promoting a more uniform distribution of the NPs and enhancing coating stability. Therefore, the XG/CE binary matrix was selected based on the complementary functions of the two components and its expected ability to improve NP stability and coating homogeneity.

Most implant systems rely on bone tissue adapting to Ra within specific ranges. Modifying an implant's surface topography can significantly enhance stability [25,31]. Ti and its alloys undergo several surface treatment methods, including thermal, chemical, electrochemical, plasma, and laser treatments. However, machining of Ti alloys presents challenges due to their low thermal conductivity and the formation of sawtooth chips [35,36]. In this context, a machining technique with varying cutting parameters was applied to achieve different roughness levels on the Ti6Al4V alloy surface. This technique offers advantages such as measurement accuracy, cost-effectiveness, time efficiency, and improved surface integrity [36]. To better understand the formation of nanocoatings on metallic surfaces, complementary techniques like CA measurement should be utilized. CA measurement provides information regarding the wettability of the coating solution on the substrate surface. The strong relationship between Ra and CA has been widely discussed in the literature [15,16,37–39].

The primary focus of this study is to enhance the surface texture for improved stability of an organic–inorganic nanostructure coating. To the best of our knowledge, this study presents the first comprehensive synthesis, characterization, and application of a novel XG/CE-ZnO binary organic–inorganic matrix as a protective nanocoating for Ti6Al4V substrates. These NPs are then coated onto a Ti6Al4V alloy substrate with varying Ra. The study examines the deposition process, the impact of substrate topography on coating adhesion, and the structural and functional properties of the nanocoatings. CA measure-

ments and electrochemical corrosion performance tests are conducted to evaluate the effect of Ra. Additionally, numerous characterization techniques are employed to analyze the morphological characteristics of the coatings. By addressing these elements, the research intends to offer detailed insight into how substrate roughness influences the morphology of ceramic–biopolymer-assisted synthesis and cost-effective organic–inorganic nanostructure coatings, ultimately aiding in the development of tailored coatings for a variety of applications.

2. Materials and Methods

2.1. Materials

XG (United State Pharmacopeia grade, purity 95%–98%, molecular weight = 600 kDa, viscosity 1200–1800 mPas) ($C_{35}H_{49}O_{29}$) was obtained from Klamar Reagent Company (Shanghai, China). Zinc nitrate hexahydrate ($Zn(NO_3)_2{\cdot}6H_2O$), CE (Celite 545 having particle dimensions between 0.02 and 0.1 mm and a density of 2.36 g/cm^3 at 20 °C), and sodium hydroxide reagent (NaOH) were sourced from Merck (Darmstadt, Germany). All materials and chemicals utilized in this study were of analytical grade and applied without further purification. The Ti6Al4V alloy was used as the substrate (composition in wt%: 6.09% Al, 3.91% V, 0.13% Fe, 0.02% C, 0.01% N, 0.01% H, 0.09% O and balanced Ti, obtained by optical emission spectroscopy). The substrate material was provided in bar form and was obtained from Varzene Metal Company (Istanbul, Turkey).

2.2. Preparation of Polymeric–Ceramic Matrix-Based ZnO NPs

Firstly, 0.025 g of XG was added to 100 mL of distilled water and dissolved thoroughly. Then, 50 mL of this solution was mixed with different amounts of CE and stirred for 30 min. To investigate the effect of CE content on the morphological characteristics of XG/CE-ZnO NPs, different CE concentrations were evaluated during the synthesis process. The synthesis parameters are summarized in Table 1. Next, 0.02 M (0.08 g in 100 mL distilled water) NaOH solution and 0.01 M $Zn(NO_3)_2{\cdot}6H_2O$ (0.297 g in 100 mL distilled water) solutions were prepared. Then, 10 mL of each salt solution was gradually transferred into the XG/CE solution during continuous magnetic stirring. The obtained mixture was sonicated using a Bandelin Sonopuls HD 3100 ultrasonic homogenizer (Germany) at 37 °C, 20 kHz and 40% amplitude. After sonication, the solution was filtered through a sterilized syringe filter with a 0.45 µm pore size. The prepared XG/CE-ZnO NPs were stored in a sterile container for later characterization and coating procedures. Following comprehensive characterization analyses, the formulation exhibiting the most suitable morphological characteristics was selected for the coating process.

Table 1. Optimization of preparation of XG/CE-ZnO NPs.

Sample Code	XG (g)	CE (g)	$Zn(NO_3)_2{\cdot}6H_2O$ (g)	Sonication Time (min)
XG/CE-ZnO NPs	0.025	0.03	0.297	30
XG/CE-ZnO (1)	0.025	0.01	0.297	30
XG/CE-ZnO (2)	0.025	0.02	0.297	30
XG/CE-ZnO (3)	0.025	0.05	0.297	30

2.3. Substrate Preparation with Different Surface Roughness

Ti6Al4V alloy substrates with dimensions of 25 mm in diameter and 2 mm in thickness were fabricated by slicing a cylindrical block. Turning processes were chosen as the method for surface structuring, given their widespread application in industry for material removal [2]. The machining operation was performed by YouJi Machine Industrial Co., Ltd. (Kaohsiung City, Taiwan) using an orthogonal surface turning process on a CNC

lathe equipped with X and Z axes, a machining stroke of 550 mm, and a rotational speed of 3000 rpm. During the cutting operation, a cutting fluid composed of water (%95) and ESTRA 320, a mineral oil-based micro-emulsion metalworking fluid (%5), was used. The DNMG 1500608-MKS insert was employed for the cutting process. After machining, all specimens were subsequently rinsed thoroughly using distilled water and ethanol, and finally dried in an oven at 60 °C. The samples were stored in a desiccator until coating. Different Ra levels were obtained by varying the feed rate while keeping the cutting speed constant at 100 m/min and the depth of cut fixed at 2 mm. The substrates were prepared using three different feed rates. In machining operations, Ra tends to increase rapidly with an increase in feed rate [40]. The surfaces of the Ti6Al4V alloy processed under feed rate conditions of 0.15, 0.25, and 0.35 mm/rev are designated as R1 (low roughness), R2 (intermediate roughness), and R3 (high roughness), respectively, with the ranking of roughness being R3 > R2 > R1. Surface roughness was measured using a Mitutoyo Surftest SJ-210 surface profilometer, and all roughness values reported in this study correspond to the arithmetic average roughness (Ra). Ra values were calculated based on five measurements.

2.4. Contact Angle Measurements of Substrates with Different Surface Roughness

The distribution of the coating solution on bare surfaces was analyzed based on Ra using CA measurement methods. This evaluation employed a low-cost and user-friendly approach supported by AI. Prior to testing, all samples underwent ultrasonic cleaning with alcohol to minimize any contamination on the surfaces. For the CA measurements, droplet images were acquired using a 10-megapixel Nikon D3000 camera at a capture resolution of 640 × 480 pixels. The photographs were taken in contrast mode and in a series. The camera was aligned perpendicular to the sample surface to ensure precise visualization of the droplet profile, and images were captured individually. All CAs were measured at 25 °C using 5 µL droplets of the XG/CE-ZnO NP solution. To minimize the influence of surface topography variations, three independent measurements were obtained from different regions of each specimen, and an average value was derived from the measurements. CAs measured from both edges of the droplet (left and right) profile were averaged to obtain the final CA value. The measurements were processed using ImageJ 1.54r in drop-analysis–LB-ADSA mode.

2.5. Preparation of XG/CE-ZnO NP-Coated Ti6Al4V Surfaces

The prepared substrate materials underwent ultrasonic cleaning in distilled water for 30 min followed by drying in an oven at 80 °C for 30 min. Solutions of XG/CE-ZnO NPs were then coated onto the treated surfaces, which exhibited varying roughness values. This was accomplished using the drop-casting method with a Pasteur pipette, where 3 mL of the solution was applied to each sample surface.

2.6. Characterization of XG/CE-ZnO NP-Coated Ti6Al4V Surfaces

The crystalline characteristics of the synthesized nanostructure were examined using an Empyrean model XRD device from Malvern PANanalytical, with Cu-Kα radiation ranging from 10° to 80° at 40 kV and 15 mA. Functional groups were analyzed between wavelengths of 400 and 4000 cm^{-1} with a VERTEX 70v model FTIR device from Bruker (Billerica, MA, USA). A Hitachi HT-7700 instrument outfitted with a lanthanum hexaboride (LaB_6) electron gun operating in an accelerating voltage range of 40–120 kV was used to undertake TEM analysis of the developed coating solution. Using red–blue–green (RGB) and independent component analysis (ICA) modes with color-corrected pictures in 8-bit format, the prepared ZnO NPs were characterized. The RGB approach was used to improve the separation and quantification of the highlighted NPs for more precise analysis

by enhancing the distinction between the NPs and the background matrix. Utilizing TEM images examined with ImageJ software and assisted by AI, the particle sizes of the prepared ZnO NPs (shown in green) were ascertained. At a resolution of 962 × 608 pixels, the TEM images were captured in RGB mode, with the green color channel being utilized for specific analysis. Prior to quantitative analysis, the images were processed using contrast enhancement, thresholding, and edge detection to improve feature visibility. Particle Analysis was employed for NP size measurements, while the Contact Angle and LB-ADSA plugins were used for droplet profile fitting and contact angle determination, providing improved measurement accuracy and reproducibility. Surface morphology and elemental mapping were analyzed using energy-dispersive X-ray spectroscopy (EDS) with a QUANTA FEG 250 scanning electron microscope (SEM) by FEI (Hillsboro, OR, USA). Ra measurements of the substrate were conducted with a Mitutoyo Surftest SJ-210 device. The stereomicroscopic examinations and microhardness analyses were performed using a YHV-50Z Digital Micro-Vickers Hardness Tester produced by YAMER (İzmir, TURKIYE) under an applied load of HV1 (1 kgf) with a dwell time of 10 s, and the hardness results were reported as the average of three separate measurements. The experimental procedures are illustrated schematically in Figure 1.

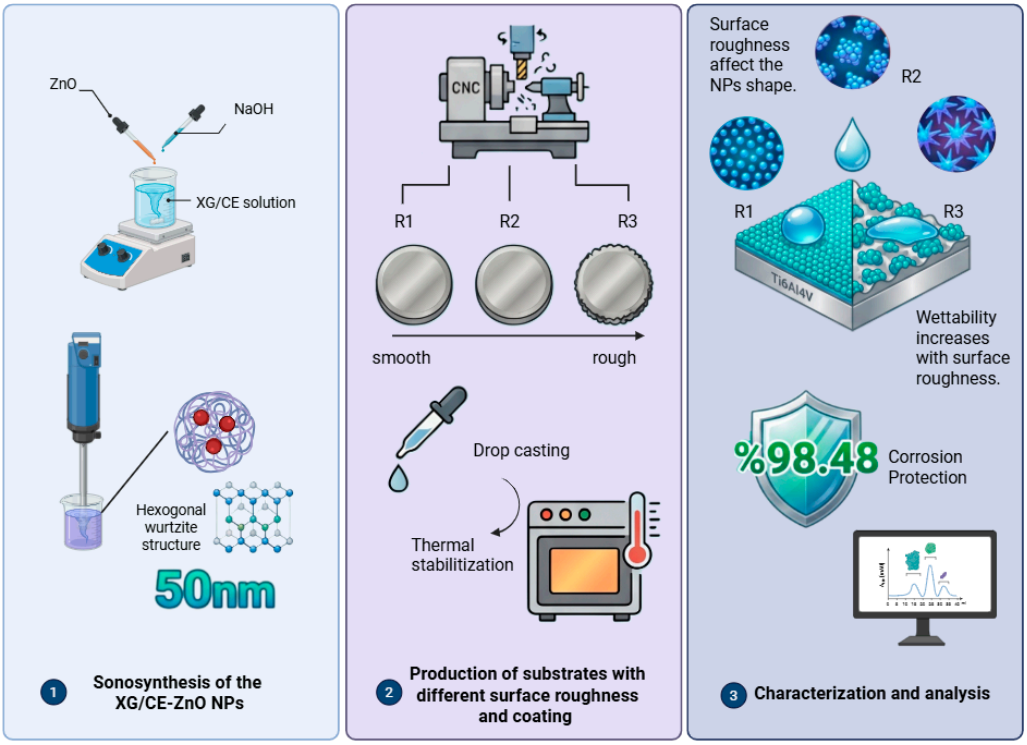


Figure 1. Schematic representation of the experimental steps of this study.

2.7. Electrochemical Corrosion Test

The anticorrosion properties of XG/CE-ZnO NP-coated Ti6Al4V surfaces with varying Ra were evaluated through electrochemical potentiodynamic polarization tests conducted at room temperature. A Gamry Interface 1000 potentiostat, interfaced with a computer, was employed for all electrochemical measurements. All measurements took place in a 1000 mL cell filled with the electrolyte. The electrolyte was Ringer's solution, and the pH of the prepared Ringer solution was measured as 5.9 prior to the corrosion tests. No further pH adjustment was performed, and all electrochemical measurements were conducted under the same solution conditions to ensure a consistent comparison among the specimens. A standard three-electrode configuration was utilized, comprising a saturated calomel

electrode (reference), a high-density graphite rod (counter electrode), and the coated sample as the working electrode. The specimens were fully embedded in epoxy resin, leaving only the coated surface (3.80 cm^2) exposed to the electrolyte, and were connected via a copper wire. Initially, the open circuit potential (OCP) was monitored until a steady-state value was reached, generally within 2 to 3 h. After stabilization, Tafel tests were performed by scanning the potential at a rate of 1.0 mV/s within a range of −250 to +250 mV relative to the OCP values. Each test was repeated three times to confirm the reproducibility of the data analyzed using software. The protection efficiency (%PE) of the coating was derived from the corrosion current density (I_{corr}) extracted from the Tafel plots, according to the equation provided in Equation (1) [41].

$$(P.E.\%) = \frac{i_{corr(bare)} - i_{corr(coated\ sample)}}{i_{corr(bare)}} \times 100 \quad (1)$$

3. Results and Discussion

3.1. Characterization Results of XG/CE-ZnO NPs

Various synthesis techniques, including microwave-assisted, plasma, hydrothermal, sonochemical, spray pyrolysis, spray drying, and gas-phase methods such as vapor transport, have been developed to prepare ZnO NPs with controlled sizes and shapes. NPs can take various forms, such as nanorods, nanowires, nanobelts, and nanostars. In the study by Mousavi et al. [42], it was reported that the crystal size, components, shape, crystal density, and morphology of ZnO NPs, particularly those with controlled shapes, significantly impact their biocompatibility and antimicrobial properties. Therefore, morphological and topographical investigations of these nanostructures are crucial for understanding their properties [43]. In this study, SEM and TEM analyses provided detailed insights into the dimensions, shape, size, and growth mechanisms of NPs. The TEM micrographs of organic–inorganic nanostructures with different CE concentrations are presented in Figure 2. The TEM images of XG/CE-ZnO NPs with varying amounts of CE demonstrated the critical role of CE concentration in determining the NPs' morphology. The TEM micrographs were acquired at different magnifications to best represent the characteristic morphology, particle size, and distribution of the NPs synthesized under each experimental condition. At a lower concentration of 0.01 g CE, the NPs were not distinctly formed, indicating insufficient support for uniform particle growth (less than 50 nm). When the concentration was increased to 0.02 g of CE, the NPs adopted an irregular spiral-like shape (less than 100 nm), suggesting partial stabilization and organization of the XG/CE-ZnO NPs. At a higher concentration of 0.05 g CE (less than 1 μm), large aggregates formed, transitioning from the nanometer to the micron scale, likely due to excessive CE leading to clustering and agglomeration. In contrast, at the optimal concentration of 0.03 g of CE, the XG/CE-ZnO NPs exhibited a desirable spherical morphology with a uniform size in the nanometer range (less than 20 nm). This concentration appeared to provide a balanced quantity of CE to stabilize the NPs without causing excessive aggregation. These findings highlight the significant influence of CE concentration on controlling particle morphology, with 0.03 g of CE deemed optimal for achieving well-defined, spherical NPs.

The mechanisms involved in the nucleation, growth, and aging of NPs are complex and require in-depth and thorough investigation. Various theories have been developed to explain these processes. Generally, the formation of NPs can be understood through several mechanisms, such as a two-step mechanism, digestive maturation, coalescence, directed assembly, and interparticle growth. Key properties of porous nanomaterials include their large surface-to-volume ratio, high porosity, and low density of additives. These materials may have diameters ranging from 10 nanometers to several hundred

nanometers, with adjustable pore sizes of 1 to 10 nanometers. Additionally, achieving well-defined particle morphology is possible, featuring regular geometries along with a very high internal surface area and pore volume. These characteristics are essential for optimizing the performance of NPs in various applications. Beköz Üllen et al. [44] reported that hybrid matrix-based ZnO NPs produced by green sono-synthesis using ginger extract were spherical in shape and smaller than 50 nanometers. Furthermore, another study indicates that ZnO NPs also exhibit a highly spherical shape [19]. This research demonstrates the impact of adding curcumin extract on the structural morphology of the NPs, as evidenced by the characterization results obtained. The study thoroughly analyzed how different concentrations of CE affect the size, shape, and agglomeration tendencies of the NPs, highlighting the influence of CE addition on the morphological properties of these NPs.

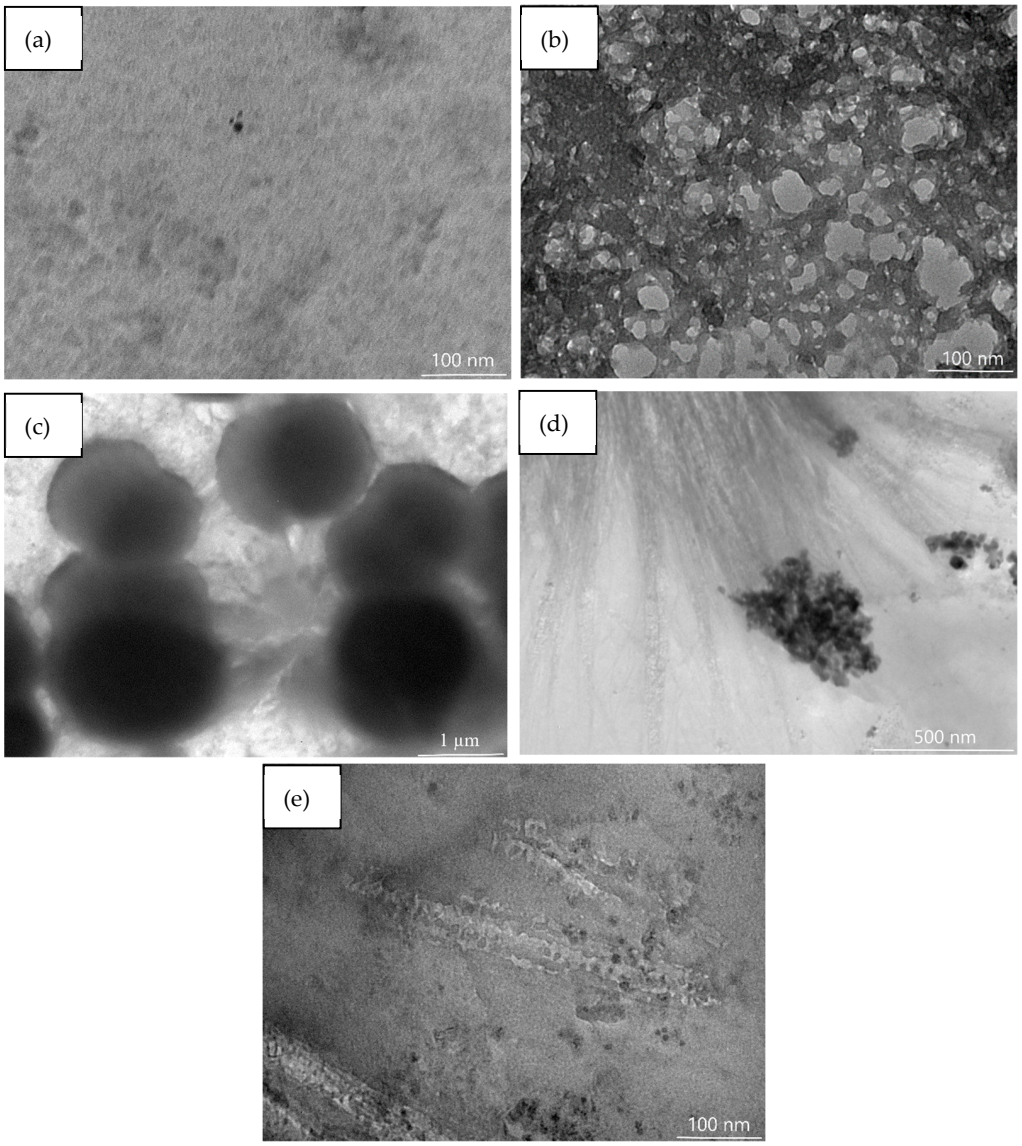


Figure 2. TEM micrographs of XG/CE-ZnO NPs with varying CE amounts: (**a**) 0.01 g, (**b**) 0.02 g, (**c**) 0.05 g, (**d**) 0.03 g (x20.000) and (**e**) 0.03 g (x60.000).

XRD analysis was conducted to investigate the chemical structure and crystallographic properties of the synthesized NPs. The XRD graph of XG/CE-ZnO NPs is depicted in Figure 3. The analysis identified characteristic peaks indicative of the crystal structures of both CE and ZnO. Peaks at 2θ = 21.80° and 26.63° correspond to the cristobalite and

quartz phases of CE, respectively [34]. Peaks at 2θ = 31.75°, 34.4°, 36.03°, 47.69°, and 56.62° correspond to the (100), (002), (101), (102), and (110) planes of ZnO NPs, respectively [45,46]. Consistently, it was concluded that ZnO NPs exhibit a hexagonal wurtzite structure [46]. These findings align with the literature, and the crystallography of ZnO and CE is compatible with the International Centre for Diffraction Data (ICDD) file numbers 01-079-0206 and 01-076-0939, respectively.

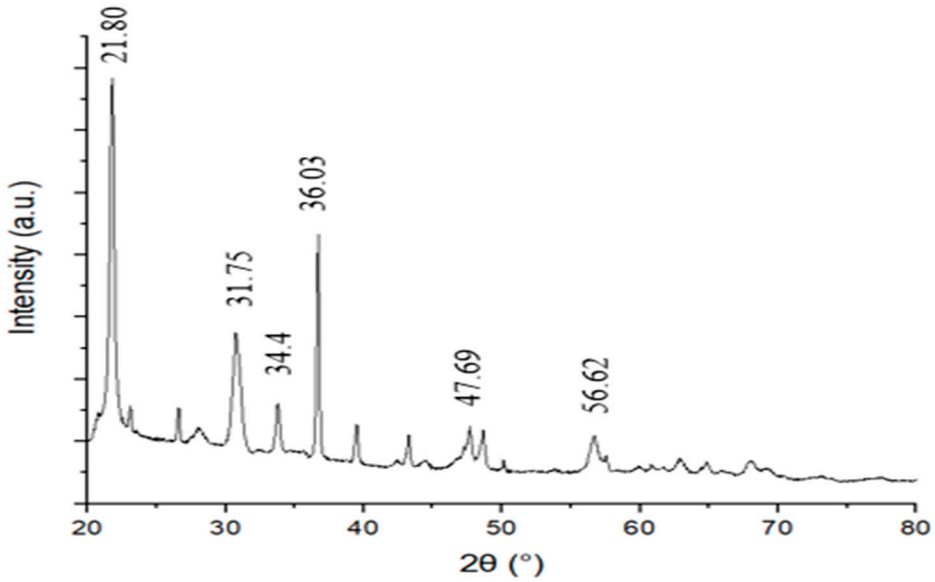


Figure 3. XRD spectrum of the synthesized XG/CE-ZnO NPs.

ZnO NP-doped XG/CE polymeric–ceramic matrix samples were characterized by the FTIR technique. The FTIR spectrum is given in Figure 4. There are broad absorption peaks at 3325 cm^{-1} (–OH) and 1635 cm^{-1} (bending of water molecules). The O–H bending vibration band occurs at 667 cm^{-1}. ZnO NPs dispersed in the XG/CE matrix are indicated by the presence of the peak in the range of 400–500 cm^{-1}, attributed to the stretching vibration of the Zn–O bond. The spectra indicate that the effect of ZnO NPs could enhance the interfacial interaction within the blend matrix [44,46–48].

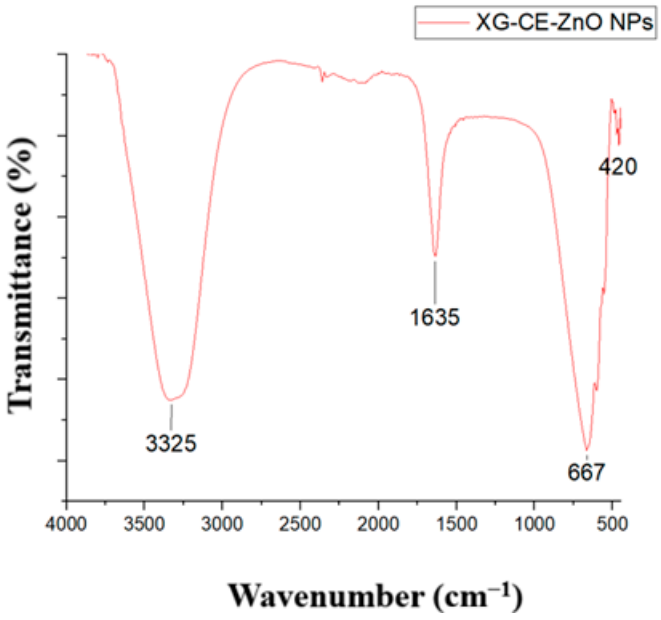


Figure 4. FTIR spectra of the synthesized XG/CE-ZnO NPs.

In this study, an XG/CE binary organic matrix blend was used as a stabilizer to produce ZnO NPs. This binary organic matrix helped control the characteristics of the particles, including their size, shape, distribution, and overall stability. Surface characteristics were examined through scanning electron microscope (SEM) images of pure XG powders and XG/CE-ZnO NPs, as shown in Figure 5. The SEM images reveal that the XG powders exhibit an irregular morphology with a rough, spongy, porous structure. In contrast, the ZnO NPs are embedded within the XG/CE organic matrix, featuring an average size of approximately 50 nm and a relatively uniform distribution, as illustrated in Figure 5b. These organic–inorganic nanostructures consist of spherical particles that are closely dimensioned. Similar findings were reported by Beköz Üllen et al. [44] regarding ZnO NPs synthesized within an organic–inorganic matrix. The nanostructures are observed to be agglomerated, a clustering likely resulting from the drying and vacuum processes during SEM imaging, as well as from the layer-by-layer deposition of the small spherical ZnO NPs. Previous studies on ZnO NPs have also reported similar outcomes in producing stable and spherical ZnO NPs using zinc nitrate combined with various organic materials [49–53]. The use of AI significantly improved the clarity of NP dispersion and aggregation patterns within the polymer matrix compared to conventional methods. For AI-related surface analysis, NP morphology data was efficiently processed and then interpreted using ImageJ software. This software enhanced our understanding of the characteristics and behaviors of the XG/CE-ZnO NPs in the organic matrix by allowing for a comprehensive analysis of their size, shape, and distribution. In the AI-enhanced SEM image displayed in Figure 5c, advanced AI algorithms applied in Rainbow RGB (8-bit) mode provide a detailed visual differentiation of key structural elements. Specifically, green highlights indicate ZnO NPs with diameters smaller than 50 nm, red indicates areas of ZnO NP accumulation on the surface, and blue represents the XG matrix. Furthermore, the 3D surface plot in Figure 5d depicts the topography of the XG/CE-ZnO NP system, illustrating variations in height and Ra using the Rainbow RGB color scheme, thereby revealing particle aggregation and distribution. This application of AI in SEM analysis was crucial for accurately understanding NP behavior and improving material characterization. The 3D surface plot was generated using the Interactive 3D Surface Plot function in ImageJ. The horizontal axes correspond to the SEM image dimensions, while the vertical axis represents grayscale intensity values rather than the actual topographical height of the NPs.

3.2. Contact Angles of Substrates with Different Surface Roughness

The interaction between a liquid and a solid surface can be quantitatively evaluated through CA measurements. Nevertheless, achieving reliable and reproducible CA values on real surfaces remains challenging due to the sensitivity of the measurements to factors such as surface heterogeneity, roughness, particle morphology, and particle size [44]. The effectiveness and uniformity of the coating are strongly influenced by several parameters, among which substrate surface preparation plays a critical role. Substrate parameters can generally be categorized into two categories: those related to surface chemistry and those related to surface topology. Key factors that influence the production of high-quality coatings include surface cleanliness (which reflects chemistry) and Ra (which reflects topology). A clean surface enhances the wetting of the coating media, while Ra provides mechanical interlocking sites for the coating. The wetting properties of the surface can be assessed using the sessile drop CA method [54]. Ra is closely linked to coatability and significantly impacts bacterial adhesion [4,25].

The degree of hydrophilicity or hydrophobicity of a surface can be determined by measuring CA. Smaller CA indicates greater spreading and better interaction between the liquid and solid surface. As the CA increases, the liquid is less able to spread on the solid

surface, making it easier for the droplet to maintain its shape. The wettability of a solid surface is closely related to several factors, including the surface energy of the solid, the surface tension of the liquid, the chemical properties, and the surface's microstructure. Consequently, the measured CA is influenced by various parameters such as the roughness and cleanliness of the surface, ambient conditions, and other contributing factors. Ra significantly affects both the CA and the wettability of the surface. This influence depends on whether the droplet fills the surface grooves or creates air pockets between the droplet and the surface. In addition to surface topography and roughness, wettability is a critical surface property that can impact the biological response to implants [15,55].

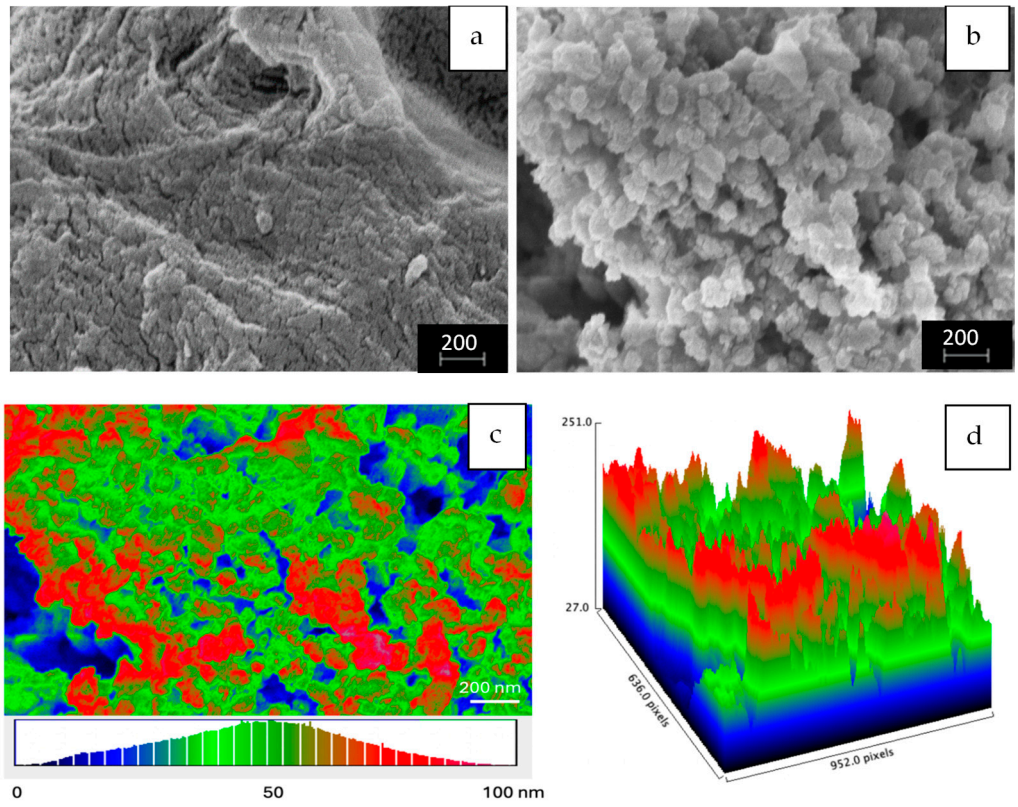


Figure 5. SEM images showcasing (**a**) pure XG, (**b**) XG/CE-ZnO NPs, (**c**) AI-enhanced SEM image of XG/CE-ZnO NPs (Rainbow RGB, 8-bit), and (**d**) 3D surface plot of XG/CE-ZnO NPs (Rainbow RGB, 8-bit).

The impact of Ra on wetting properties was evaluated through CA measurements. Figure 6 provides a visual representation of how CA values change with increasing Ra values. As illustrated in the images, the distribution of the coating solution became more challenging as the Ra values increased. The average CAs measured for the samples coded R1, R2, and R3 were 61.5°, 58.8°, and 48.6°, respectively. Since all measured CAs on the sample surfaces are below 90°, these surfaces can be classified as hydrophilic, demonstrating wetting behavior. As the Ra value of the Ti6Al4V alloy substrates increases, the CA decreases, thereby enhancing the surface's hydrophilicity and promoting greater droplet spreading. For an effective coating, it must achieve a "Wenzel" state, meaning that the coating material should cover the entire surface, completely eliminating any air pockets [56]. This is characterized by a sufficiently low CA (<90°) and surface features that do not cause the liquid to become pinned. The observed reduction in CA with increasing Ra can be attributed to the droplet spreading along the surface grooves [38]. Even minor variations in Ra can significantly improve wetting behavior. The presence of micro- and nanoscale hierarchical structures on roughened surfaces creates a topography that can

effectively trap the coating material [57]. Additionally, the CAs for Ti-based alloys with different roughness levels reported by Beköz Üllen et al. [44] were consistent with those found in this study. It has been established that surface wettability, a critical requirement for Ti-based alloy implants, is heavily influenced by Ra and the morphology of the coatings.

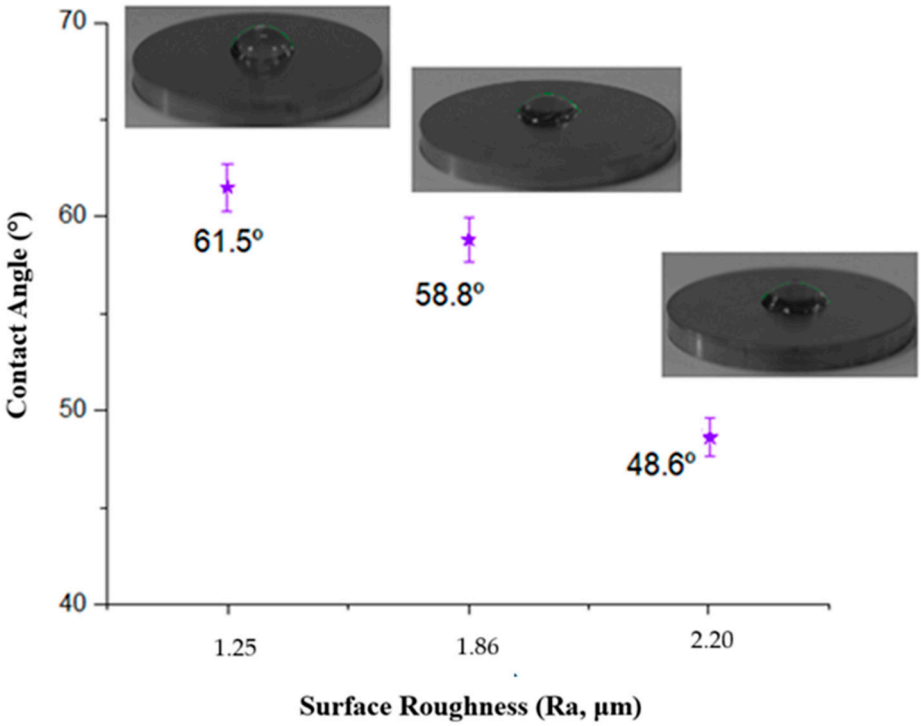


Figure 6. The change in CA with NPs at different Ra.

Increasing the roughness of the biomaterial surface enlarges the surface area, which improves implant adhesion at the implantation site and positively influences bone formation [58]. Surface treatments of implant materials affect their surface energy and CA, mainly by altering the Ra. The adhesion of the implant to the surrounding tissue is largely dependent on these factors. Previous studies consistently show a relationship where increasing Ra leads to a reduction in CA [55,59,60]. These findings regarding CA and Ra align with earlier research in the literature [38]. After applying surface modification processes aimed at enhancing the integrity of implant materials, it is important to measure Ra and CA to ensure optimal bonding characteristics. Therefore, following surface processes that improve implant–bone integration and especially alter surface composition, both surface energy and CA should be measured. An optimal relationship should be established among these values and Ra for different surface processes. Surface preparation through mechanical methods typically eliminates residues from the metal surface while increasing surface area through induced roughness. Enhancing the surface area of metal-based materials, which usually have a primary oxide layer, promotes the formation of an additional oxide layer. Since the wettability of a surface primarily depends on its outer atomic layer, an increase in oxide thickness linked to rougher surfaces decreases the CA [61,62]. This observation is supported by Kietzig et al. [63], who note that a rough metal surface contains numerous active centers, making it likely that an increase in the surface profile will lead to a reduction in the CA. As a result, it has been determined that variations in Ra and the surface properties altered by nanostructuring significantly impact both the CA and surface wettability. They stated that the rough metal surface contains numerous active centers and therefore an increase in surface profile has a high probability of reducing CA. As a result, it has been

determined that variations in Ra and the surface properties altered by nanostructuring significantly impact both the CA and surface wettability.

3.3. Characterization of XG/CE-ZnO NP-Coated Ti6Al4V Surface

3.3.1. Surface Roughness Results

Ra, along with both macro- and microscale structures, plays a crucial role in determining the surface energy and biocompatibility of metallic biomaterials. The topography and roughness of these materials are key factors that influence cell adhesion, proliferation, and growth. Various properties of implants, such as geometry, design, and connection, also affect their osseointegration, which is critical for effective bone bonding and overall implant performance. Among these factors, the average roughness of implants is a vital determinant of both short-term and long-term clinical outcomes, as well as the sustainability of the manufacturing process. The Ra parameter impacts several material characteristics, including surface wear, chemical durability, and microhardness [2,25,31,64,65]. The primary goal of roughening or processing implant surfaces is to provide cellular activity and improve bone apposition [31]. Therefore, it is essential to assess changes in Ra properties before and after coating. For these reasons, conducting comprehensive studies on surface modifications, such as machining and coating of Ti6Al4V alloy, one of the most frequently used biomaterials for implants, is important. In machining operations, cutting parameters significantly affect the Ra value. By carefully selecting machining conditions, such as cutting speed, feed rate, and depth of cut, it is possible to ensure that the manufactured parts meet the required dimensional precision and surface finish standards [35,36]. A comparison of the average Ra values for uncoated Ti6Al4V samples with varying roughness levels and their coated counterparts is presented in Table 2. The Ra values were measured for the Ti6Al4V alloy surface after varying the feed rates during turning. The results showed that increasing the feed rate from 0.15 mm/rev to 0.25 mm/rev led to a 32.79% increase in the Ra value. A further increase to 0.35 mm/rev resulted in a 43.18% rise. These findings indicate a significant correlation between the average Ra values and the feed rate; as the feed speed increases, the Ra value also increases. Several researchers have reported that higher feed rates during machining of the Ti6Al4V alloy lead to elevated Ra values [2,35,44]. Multiple studies have indicated that the Ra value is influenced by the feed rate, sometimes referred to as the secondary speed [35]. Moreover, increasing the feed rate during turning results in higher temperature and pressure at the cutting edge. While changes in the processing conditions of the Ti6Al4V alloy do not affect the strength of the part, they do impact the cutting edge. The elevated temperature can cause chip adhesion on the cutting edge, negatively affecting the surface quality of the machined material. In summary, the study demonstrated that increased feed rates raise the temperature and pressure at the cutting edge, adversely impacting chip formation and surface quality, which ultimately leads to an increase in the Ra value [35,66]. Hagen et al. [2] noted that optimizing cutting parameters could result in machining surfaces that provide protective coatings with a longer lifespan. Beköz Üllen et al. [44] achieved the desired Ra for Ti-based parts used in coating with ZnO NPs by adjusting the feed rate during lathe cutting. This study frequently employed turning for machining the Ti6Al4V alloy due to its advantages in optimizing machining parameters, achieving dimensional precision, and maintaining surface integrity. The surface topography, which influences the interfacial interaction between the bio-implant and surrounding bone tissue, is primarily determined by the average roughness value and its orientation [67]. Ra values for implants can be categorized into nano-, micro-, and macroscale structures based on the dimensions of their features [31,68]. Typically, the roughness of metallic biomaterials is assessed at the microscale. This microscale can be further divided into medium and fine roughness, where “fine” is defined as a Ra of 0.5–1 μm, and “medium” ranges

from 1 to 2 µm [12,69,70]. Notably, all our Ra values, except for the uncoated Ti6Al4V part labeled R3, fall within the medium scale of 1–2 µm.

Table 2. The average roughness value of coated and uncoated surfaces.

Sample Code	Uncoated, µm	Coated, µm	Difference, %
R1	1.25 ± 0.13	1.11 ± 0.11	−11.2
R2	1.86 ± 0.18	1.55 ± 0.19	−16.6
R3	2.20 ± 0.24	1.89 ± 0.17	−14.1

The part coded R3 falls within the medium scale range after coating. The coating process did not significantly alter the Ra values of samples that originally had medium roughness. Jiang et al. reported that the Ra values measured after coating remained comparable to those obtained prior to the coating process, underscoring the importance of this observation for maintaining chemical stability [71]. Based on these findings, the post-coating Ra values remain in the medium range, suggesting potential suitability for biomedical applications. Alla et al. [31] noted that a higher Ra value is desirable for the surfaces of metal-based biomedical devices, as it helps prevent bacterial interaction by enhancing cell adhesion, spreading, and growth. In our previous study, Ra values of Ti-based substrates of 1.247 µm, 1.825 µm, and 2.186 µm before coating were reported, and these were measured to be 1.018 µm, 1.526 µm, and 1.92 µm after ZnO NP coating, respectively [44]. In another study, the Ra values before and after coating were determined to be 1.281 µm and 1.023 µm, respectively [12]; in a separate study, the roughness decreased from 1.896 µm to 1.672 µm [6]. The consensus from these studies is that nanocoatings tend to reduce roughness in micrometer increments. Based on these perspectives, the roughness values obtained in the present study are also considered significant. In this study, Ra values after coating decreased by 11.2%, 16.6% and 14.1% in parts with different roughness codes R1, R2 and R3, respectively. The smoothing effect of coating is less pronounced on rough surfaces. Beköz Üllen et al. [44] reported that Ra values decreased by approximately 12%–18% after applying a ZnO nanocoating on Ti-based substrates. This reduction in roughness was found to diminish as the initial roughness increased. Hagen et al. explained that an increase in the Ra raises the peak-to-valley height, which subsequently reduces delamination and improves the effective contact area of the coating [31]. Ra measurements indicated that the Ra value of the coated surfaces was lower than that of the uncoated parts. Several studies suggest that the observed decrease in Ra after coating results from the microscale measurement approach, as the coated particles are at the nanometer scale [10,44]. Therefore, the reduction in Ra can primarily be attributed to the incorporation of NPs in the coating, along with the fact that measurements were conducted at the micron scale.

The discovery that rougher implant surfaces with a higher surface area improve contact between bone and the implant has driven researchers to explore biomaterials with varying average roughness values [31]. Studies involving intraosseous dental implants with different Ra values have shown that rough surfaces integrate more effectively with bone [58]. Typically, Ra values for the micro-surface topographic profiles of implants range from 1 to 10 µm. Recent research has also concentrated on the relationship between surface integrity and nanoscale modifications, especially concerning Ti6Al4V alloy implant surfaces. Understanding the interaction between surface processing operations and the resulting Ra is crucial [68]. This study offers insights into how different surface treatment procedures affect the Ra achieved after processing. The next section will address the effects of changes in Ra on the micro- and macrostructure and, on a broader scale, the microhardness properties of the surface.

3.3.2. Microstructural Characterization Results

Rough surfaces provide a greater surface area for the distribution of NPs compared to smooth surfaces. As the Ra changes, the size, shape, and quantity of nanostructure clusters formed on the surfaces also vary due to changes in microstructural and surface chemical composition [32,70,71]. Figure 7 presents SEM images and EDX spectra of Ti6Al4V substrates prepared with different Ra levels. The results from the SEM and EDX analyses indicate that the XG/CE-ZnO NP coating is highly uniform and compact, displaying smooth surface morphology without visible defects such as microcracks or holes. In Figure 7a, ZnO NPs are evenly distributed on the surface within a relatively homogeneous size range. They are close to spherical in shape, and agglomeration is less pronounced compared to other samples, resulting in a clearly smooth coating on the Ti6Al4V surface with a roughness average of 1.11 µm. In Figure 7b, some randomly agglomerated coating particles are visible on surfaces with a Ra of 1.55 µm. These agglomerated particles adhere to the surface, creating an irregular surface morphology. The SEM image of the coated R2 sample shows that the NPs change shape from spherical to needle-like forms as the degree of agglomeration increases. In Figure 7c, with an increase in Ra to 1.89 µm, the shapes of the nanostructures attached to the surface evolve, resulting in agglomerated NPs forming star-like structures. This underscores the importance of substrate surface characteristics in determining coating growth and NP morphology. In a related study carried out by Beköz Üllen et al. [44], a biopolymeric matrix was employed to control particle size, promote homogeneous distribution, and enhance structural stability. The study demonstrated that the average surface roughness (Ra) of the titanium-based substrate significantly affected the morphology of the deposited coating, with higher Ra values leading to a more pronounced presence of organic–inorganic matrix-based ZnO NPs within the coating layer. According to Paknahad and Nogorani, increased roughness reduces the number of available reaction sites and induces a cauliflower-like morphology, which supports the development of star-like features on rough surfaces [30]. Bernard et al. noted that the surface topography of the substrate plays a crucial role in governing the microstructural characteristics of coatings. Consistent with this observation, the present study revealed that substrates with different roughness values produced coatings exhibiting variations in both column size and column density [72]. Caio and Moreau [73] also reported that variations in substrate roughness lead to structures with differing peak sizes, suggesting that higher roughness values encourage the formation of a greater number of columns. The coating material exhibited a fully needle-like morphology. These findings confirm that the surface characteristics of the substrate significantly affect coating growth, playing a key role in controlling the size, shape, and distribution of NPs. The coatings were free of cracks and gaps, indicating successful deposition, which aligns with research emphasizing the impact of substrate surface structure on coating morphology [30,73]. In NP synthesis processes and applications, there is a direct relationship between fundamental geometric shapes and Ra. Ra does not determine the shape of the NPs; rather, it is a result of shape irregularities, crystal structure defects, and external morphological protrusions. The shape of the NPs (spherical, rod, plate, star, etc.) depends on the synthesis method used, the temperature, and the chemical additives. Ra is closely associated with NPs' morphology and plays a significant role in determining their structural and functional characteristics. Several key mechanisms govern the relationship between particle shape and Ra. First, crystallization defects that arise from differences in atomic arrangement, crystal growth rate, and local surface energy during particle formation often result in anisotropic morphologies with rough, irregular, or sharp-edged surfaces. Second, although Ra does not fundamentally alter the overall geometry of a particle, it substantially increases the effective surface area beyond that predicted by its geometric dimensions, thereby influencing surface-related phenomena such as adsorption, catalytic

activity, and interfacial interactions. Third, particles with rough or irregular surfaces exhibit enhanced mechanical interlocking compared to smooth particles, promoting aggregation and cluster formation in liquid media due to increased physical interactions between neighboring particles. The extent and nature of Ra also vary according to NP morphology. Spherical NPs generally exhibit relatively smooth surfaces because their isotropic growth minimizes surface irregularities. Nevertheless, rapid cooling or non-equilibrium synthesis conditions may introduce nanoscale pits, indentations, or microcracks on their surfaces. In contrast, nanowire structures typically possess greater Ra owing to their anisotropic crystal growth, with their tips and edges exhibiting pronounced surface irregularities. Similarly, polyhedral NPs display higher roughness at corners and edge junctions, where elevated surface energy promotes the formation of crystallographic defects and localized surface asperities compared with the smoother crystallographic facets [74,75]. Moreover, it is known that NPs in various forms can provide diverse functional properties to surfaces [76]. SEM-EDX analysis of Ti6Al4V surfaces coated with XG/CE-ZnO NPs revealed signals for carbon, oxygen, zinc, and silicon, along with characteristic substrate peaks (Figure 7a–c), consistent with previous literature findings [30,44]. Mechanical stress generated in the coating structure at the nanoscale causes compression or expansion of the crystal structure in the material, altering the interatomic distance and potentially having small effects on bonding energies. This can cause changes in the energies of specific element peaks in the EDX spectrum. Furthermore, the bonding of atoms in a molecule or crystal structure affects the outer electron clouds. This can sometimes cause shifts in the peaks [77].

3.3.3. Macrostructure and Microhardness Results

The macro images and microhardness measurements of the bare and coated surfaces are presented in Table 3. The macro images indicate that an increase in substrate roughness influences the macroscale morphology of the coating. The surface topography exhibited a non-uniform distribution of irregular grooves and protrusions [77]. Different levels of Ra are clearly visible in the images of the uncoated surfaces. The distribution of the coating on the surface can be observed in the stereomicroscope images, which clearly show that the surfaces have been coated successfully. Sample R1 exhibits a relatively small size distribution, while larger sizes are noted in the other samples. Optical micrographs revealed the presence of microscale channels and groove-like surface features resulting from the machining process. The morphology, dimensions, and distribution ratio of these grooves can be tailored through varying the processing parameters. In a similar study by Beköz Üllen et al. [44], it was emphasized that the macroscale morphology changed after the application of nanocoating, correlating with an increase in substrate roughness. Their findings indicated that the altered substrate roughness following the machining process led to the formation of microscale channels and grooves. Caio and Moreau [73] reported that implant surfaces incorporating microscale grooves or channel-like features enhance bone formation under both in vitro and in vivo conditions. This supports our study's findings regarding the controllability of groove structure. Some research has suggested that Ra contributes to the formation of a columnar structure on the surface [25]. When examining the changes in hardness, it was noted that residue was present in all samples after coating. The enhancement in surface hardness can be attributed to the incorporation of CE, a rigid siliceous ceramic material, and ZnO NPs, which reinforce the coating matrix and improve its resistance to localized deformation. Although an increase in hardness was observed across all samples, the highest increase occurred in sample R1. While machining is primarily a surface treatment technique, it can also be used to create specific surface topographies and compositions. The properties of machined surfaces are primarily influenced by the machining parameters of the workpiece [31]. The machining process, driven by the insert,

creates aligned valleys and grooves on the surface due to the plastic deformation of the outer layers. Variations in Ra values, resulting from different processing parameters, lead to the production of distinct macrostructures in this investigation. Paknahad and Nogorani et al. [30] deposited NPs on the surface that preferentially accumulated within the deeper regions of substrate surface scratches. Their study also highlighted that as Ra increases, NPs are more likely to form clusters. In a similar investigation, the impact of changing the roughness of Ti-based substrates on the properties of ZnO nanocoatings was examined [44]. The researchers found that the topography of the coating surfaces exhibited a non-uniform distribution of irregular grooves and peaks. As it is challenging to study the effects of macro-morphological surface changes on various properties, conducting a micro-morphological evaluation is crucial.

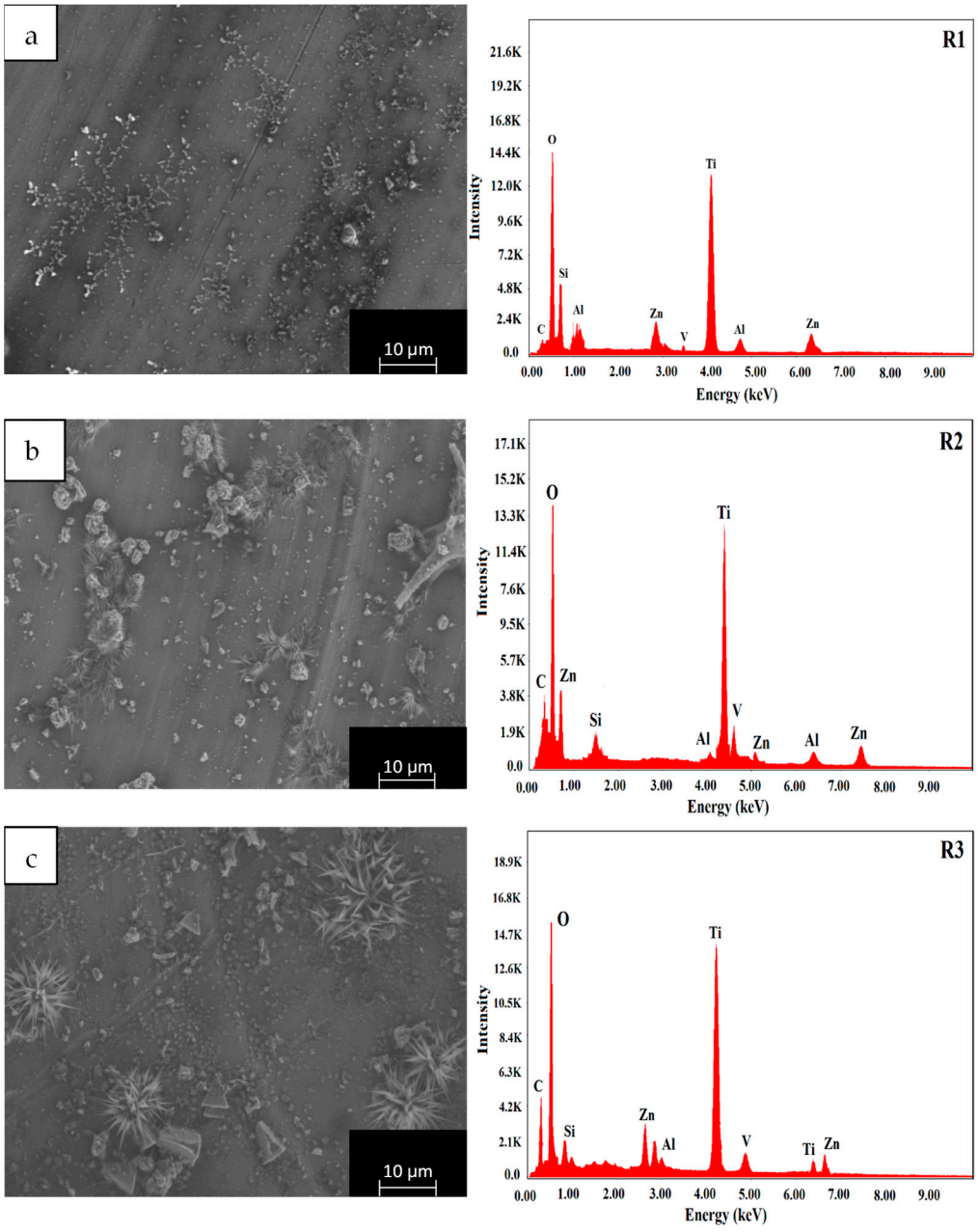
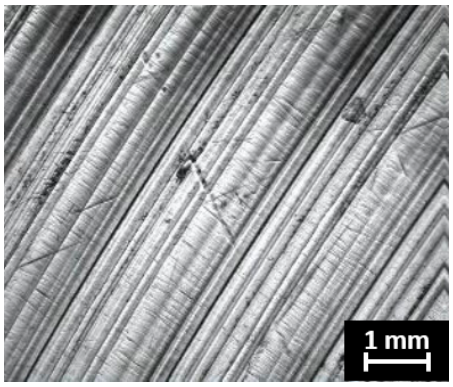
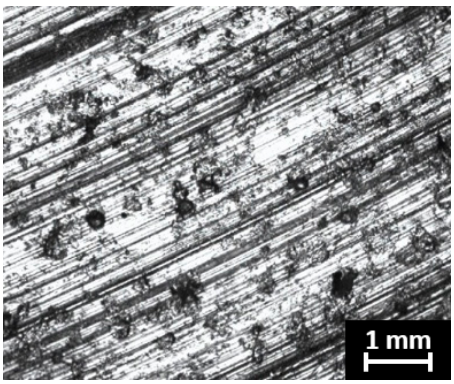
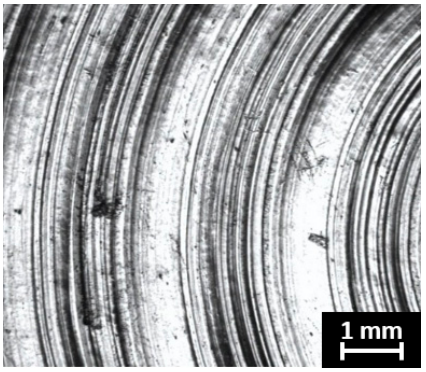
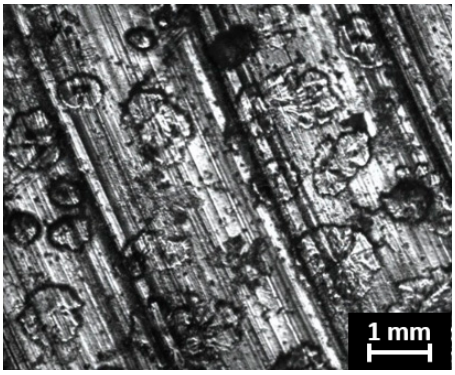
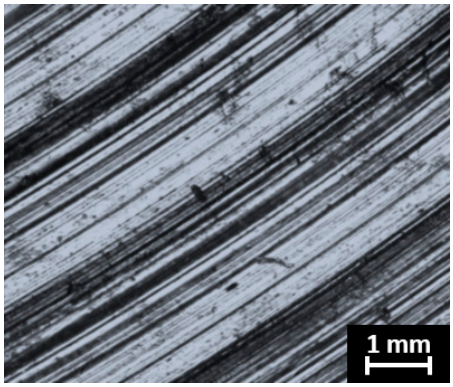
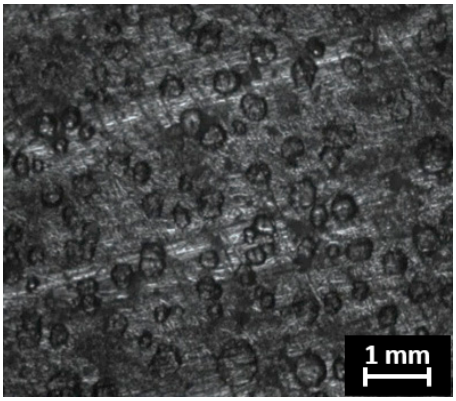


Figure 7. SEM images and EDX results of the coated surfaces at different Ra values: (**a**) R1, (**b**) R2, and (**c**) R3.

Table 3. Substrate roughness influences macrostructure and microhardness on uncoated and coated surfaces.

Sample Code	Uncoated Surface	Coated Surface	Increase (%)
R1	 308.4 ± 10.5 HV1	 358.3 ± 11.7 HV1	16.2
R2	 337.6 ± 13.7 HV1	 367.7 ± 14.3 HV1	8.9
R3	 354.5 ± 13.7 HV1	 376.4 ± 13.9 HV1	6.2

3.3.4. Electrochemical Corrosion Test Results

The anticorrosive properties of titanium-based implants are essential for their successful use in medical applications. One of the main challenges is ensuring the long-term stability of these metallic implants under corrosive conditions, which can be addressed using various surface modification techniques [78]. Research indicates that Ra and coating defects are significant factors impacting corrosion performance [79]. Common surface engineering methods such as roughening, machining, and coating are employed to improve the biological and chemical performance of implants. These improvements increase service life by boosting bioactivity, wettability, osseointegration, and corrosion resistance [80,81]. In implantology, the success of metallic biomaterials relies on the balanced interplay of

three key, intrinsically linked parameters: (i) surface roughness, (ii) biocompatibility and osseointegration, and (iii) corrosion performance. In terms of surface roughness and osseointegration, the macro-, micro-, and nano-level roughness on the implant surface creates a large surface area for bone cells (osteoblasts) to adhere to. Appropriate roughness (average 1–2 μm Ra) increases surface energy, ensuring excellent blood flow (wettability) to the implant surface. This is the first and most critical step for successful bone formation.

Additionally, among various metal oxide-based nanostructures, ZnO NPs have attracted considerable attention for their excellent corrosion-inhibiting properties. Studies show that zinc in ZnO can help reduce bone loss by promoting bone formation and enhancing the mineralization of osteoblasts [82]. Surface corrosion resistance is a crucial property for implants, and it has been shown to be highly dependent on the roughness average (Ra) and the morphology of coatings [80,81,83]. Surface integrity creates direct pathways between the corrosive environment and the substrate, which is vital for the barrier function of these coatings. However, limited research has been conducted on the impact of ZnO NP coatings on the corrosion resistance of various substrates [79,84,85]. It is evident that the XG/CE-ZnO NP coating reduces direct environmental interaction by forming a physical barrier on the metal surface. Additionally, the literature suggests that corrosion resistance may be enhanced by the spherical structure of the NPs. The surface integrity of coatings made with an organic–inorganic blend matrix of NPs is important for improving corrosion resistance. To the best of our knowledge, the anticorrosive performance of XG/CE-ZnO NP coatings on Ti6Al4V substrates has not been previously studied. This research aims to investigate the corrosion resistance of XG/CE-ZnO NP coatings and how the roughness average influences their performance. Ultimately, the primary objective is to improve the corrosion properties of the Ti6Al4V alloy with surface modification strategies, thereby enhancing its service life and reliability in biomedical applications.

In this regard, the electrochemical behavior on the substrate surfaces with different roughness is investigated using the electrochemical potentiodynamic polarization method. Figure 8 displays (a) the OCP results and (b) the polarization curves derived from Tafel extrapolation, illustrating the corrosion behavior of both uncoated and coated specimens. The corrosion potential (E_{corr}) and the corrosion current density values (I_{corr}) evaluated directly from the polarization curves using the Tafel extrapolation method are given in Table 4. When examined in detail, OCP curves (Figure 8a) are the curves used to evaluate the stable condition in the tested solution, and it is interpreted that the samples on top are in a more stable condition. In this case, R1 samples with less Ra showed better stabilization in both coated (−0.144 V) and uncoated (−0.339 V) conditions. After the organic–inorganic blend matrix-based ZnO NP coating, stabilization increased in all samples. Larger E_{corr} and smaller I_{corr} normally indicate better corrosion resistance [6]. From the polarization curve data, it is evident that XG/CE-ZnO NP-coated samples showed enhanced electrochemical behavior, characterized by higher corrosion potential and lower current density than the uncoated samples with similarly rough surfaces. This finding indicates that surface nanomodification may effectively enhance the corrosion resistance of the Ti6Al4V substrate.

In the examinations conducted of Tafel curves (Figure 8b) formed after electropolarization, it is observed that corrosion behavior decreases due to increasing Ra. However, after coating, protection of over 95% was detected in all samples. The sample with a Ra of approximately 1.000 μm has the highest corrosion resistance because it gains passivation of 98.48% after coating. As shown in Figure 8b, all coated samples exhibited more positive E_{corr} values and significantly lower Icorr values compared to the bare substrate. The corrosion potential of the coated samples shifted towards a more noble direction, indicating enhanced anodic protection for the Ti6Al4V substrate in Ringer's solution. This finding highlights the significance of synthesized NPs in improving corrosion resistance.

Based on the CA results from this study, varying surface morphologies led to differences in surface wettability. Compared to the samples coded R3, the lower roughness average of the R1-coded samples may be attributed to reduced surface hydrophobicity. Changes in Ra that affect microstructural properties and surface wettability will inevitably influence the corrosion characteristics [86–88]. The electrochemical measurements clearly show that the coated R3 sample exhibits higher corrosion susceptibility compared to the coated R1 and R2 samples. The differences in corrosion resistance associated with roughness can be attributed to several factors. First, the reduction in Ra due to the coating may hinder the penetration of aggressive electrolytes, thereby slowing down the corrosion process. Second, the diffusion of water, ions, and potentially corrosive agents is influenced by the total path length available for their movement at the interface. Therefore, a smoother interface may decrease compositional heterogeneity, further enhancing corrosion resistance [56,86].

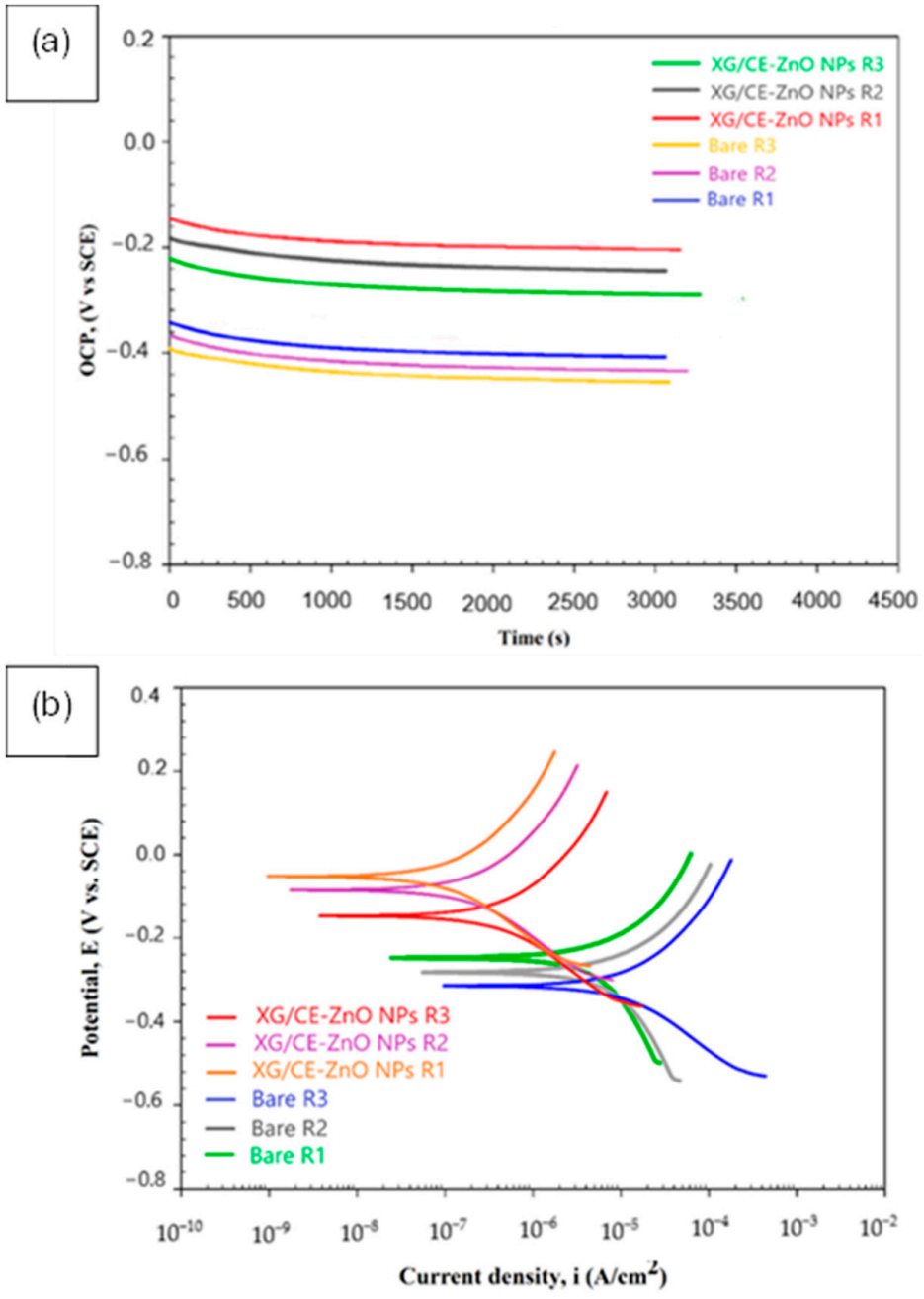


Figure 8. Electrochemical corrosion test results of the uncoated and coated substrates with different roughness: (**a**) OCP and (**b**) Tafel graph.

Table 4. Results obtained from the potentiodynamic polarization curves for the bare and coated substrates.

Sample Code	OCP (V)	E_{corr} (mV)	I_{corr} (μA/cm^2)	Protection Efficiency P.E. (%)
Bare R1	−0.339	−243	4.163	-
Bare R2	−0.362	−273	6.849	-
Bare R3	−0.388	−315	8.438	-
XG/CE-ZnO R1	−0.144	−54.3	0.063	%98.48
XG/CE-ZnO R2	−0.181	−80.4	0.125	%98.17
XG/CE-ZnO R3	−0.22	−150	0.406	%95.18

Surface modifications alter the mechanical, chemical, and topographic properties of implant surfaces. The application of an XG/CE-ZnO NP coating on the Ti6Al4V alloy, with varying roughness, enhances uniformity, which plays a critical role in maintaining chemical stability. The improvement in corrosion resistance is attributed to the synergistic action of several mechanisms. The XG/CE-ZnO NP coating acts as a physical barrier that reduces the direct interaction between the electrolyte and the Ti6Al4V substrate. Furthermore, the incorporation of CE and ZnO NPs enhances the compactness and structural integrity of the coating, thereby limiting the formation of defects that can serve as pathways for corrosive species. In addition, smoother substrates promote more homogeneous coating morphology, reducing NP agglomeration and coating discontinuities. The combined influence of these factors suppresses electrolyte penetration and contributes to the enhanced corrosion resistance observed in the coated specimens [89,90]. Potentiodynamic corrosion tests revealed that the corrosion currents of uncoated Ti6Al4V alloy samples were higher than those of the coated samples, indicating that the corrosion resistance of the coated implants was significantly improved. The ZnO NP coating applied to biomedical materials notably enhances the lifespan of implants in terms of both strength and corrosion resistance. However, defects on the coating surface, such as cavities and cracks, can create pathways for corrosive solutions to penetrate, which ultimately reduces corrosion resistance [6]. The coated surfaces R1 and R2 exhibited the highest corrosion potential values, indicating a minimal chemical affinity. As presented in Table 4, the corrosion current densities show that all coated samples, particularly those enhanced with NPs, exhibited significantly reduced corrosion rates compared to the uncoated substrate. The higher corrosion rate observed in the coated R3 samples, as compared to the coated R1 samples, may be attributed to the presence of agglomerated NPs on the surface. This agglomeration can negatively impact the protective properties of the coating, leading to the formation of voids and porosity within these deposits. Additionally, samples with a lower roughness average demonstrated higher corrosion resistance due to their smoother surface. Thus, it can be concluded that the inclusion of ZnO NPs significantly influenced Ra values, thereby enhancing corrosion resistance. Kuang et al. [89] reported that coatings can effectively prevent the penetration of corrosive ions in the electrolyte. Again, in the same study, it was stated that corrosion products formed by a decrease in the hydrophobic effect of the surface destroyed the micro-nanostructure and caused a decrease in corrosion resistance. In the present study, by decreasing the substrate roughness, the microstructural feature of the nanocoating was modified, which results in its enhanced corrosion resistance. Despite the potential improvement in coating adhesion associated with rougher surfaces through mechanical interlocking, smoother surfaces exhibited more homogeneous coatings and consequently better corrosion resistance [90].

Wang et al. [91] have suggested that the corrosion behavior of coated surfaces can be explained by the interplay between the Ra and CA. As a general trend, optimal Ra improves

both coating durability and corrosion performance, while surfaces that are either too smooth or too rough tend to impair corrosion performance, thereby decreasing coating durability. The OCP response of rougher Ti6Al4V surfaces is observed at a lower potential than that of smoother surfaces. This phenomenon is likely caused by pronounced indentations in the passive layer, which compromise surface stability and require continuous oxide repair to maintain protection [92]. Paknahad et al. [30] reported that an increase in Ra led to a notable rise in the I_{corr} value of the bare substrate, while a slight decrease in I_{corr} was observed following coating. Furthermore, it has been suggested that Ra decreases the corrosion performance of stainless steel, particularly in chloride-rich environments, as surface irregularities and grooves serve as accumulation sites for chloride ions, thereby promoting localized corrosion. Saidi et al. [80] showed that localized corrosion on ZnO NP-coated Ti6Al4V substrates triggered low-frequency responses due to load transfer effects. The diminished corrosion performance was explained by the high roughness of the coatings, leading to an increased effective exposed area. This study provides a new strategy and perspective for coating organic–inorganic nanostructures on Ti6Al4V alloy implants. The measured potentiodynamic polarization results showed that significantly better uniformity and corrosion resistance were achieved with the coating on the substrate in relation to the Ra.

4. Conclusions

The surface of Ti6Al4V alloys with varying roughness was modified using a novel combination of XG/CE-ZnO NPs. Comprehensive investigations were conducted to explore superficial properties, enhance the corrosion performance of the organic–inorganic nanostructures coated on the Ti6Al4V surfaces, and improve their applicability in the biomedical field. The results can be summarized as follows:

- The TEM results demonstrated that CE concentration significantly influenced the morphology and size of XG/CE-ZnO NPs. At the optimum concentration of 0.03 g CE, stable NP formation of balanced CE levels was achieved, and uniform spherical NPs were obtained. ZnO NPs were well dispersed in the XG/CE clay organic matrix, with an average size of approximately 50 nm and a spherical shape. ZnO NPs showed a hexagonal wurtzite crystallographic structure.
- Different Ra values were obtained using the turning technique, which is cost-effective, provides good dimensional accuracy, and maintains surface integrity. In the turning process, Ra values increased with increasing feed rate.
- Ra values of the surface-modified Ti6Al4V alloys decreased by approximately 12%–18% after coating them in all samples. The improvement in surface smoothness after coating is less pronounced on specimens with initially rough surfaces.
- With the increasing Ra value of Ti6Al4V alloy substrate surfaces, the CA decreases and the spreading behavior of the droplet increases.
- The chemical composition of the coating surface was essentially consistent across specimens, regardless of differences in Ra.
- After nanocoating, an increase in microhardness was observed on the surface of all samples. The increase in substrate roughness influenced macroscale morphology. Smooth surfaces with decreasing Ra values provided better corrosion protection. After coating, Ti6Al4V substrates showed a more positive Ecorr and a lower Icorr.
- By optimizing cutting parameters, machining can provide surfaces with long-lasting protective nanocoatings.
- The findings of this study could support the development of innovative methods and materials for the modern design of implantable medical devices featuring nanostructured surfaces.

- Improving the long-term corrosion resistance of Ti6Al4V implants remains a major challenge that requires the application of various surface modification strategies. Our future research goals include applying different strategies, such as surface texturing and coating applications, to prevent shortened service life of the implant and improve its performance by enhancing bioactivity and antibacterial activity.

Author Contributions: Conceptualization, Ş.A., N.B.Ü., G.K.Ş. and S.K.; methodology, N.B.Ü., G.K.Ş. and S.K.; validation, Ş.A. and N.B.Ü.; formal analysis, N.B.Ü. and G.K.Ş.; investigation, Ş.A., N.B.Ü., G.K.Ş. and S.K.; writing—original draft preparation, Ş.A., N.B.Ü., G.K.Ş. and S.K.; writing—review and editing, Ş.A., N.B.Ü., G.K.Ş. and S.K.; resources, S.K.; supervision, N.B.Ü.; project administration, N.B.Ü.; funding acquisition, Ş.A. All authors have read and agreed to the published version of the manuscript.

Funding: This publication was supported by the Scientific Research Projects Coordination Unit of Istanbul Yeni Yuzyil University.

Institutional Review Board Statement: Not applicable.

Informed Consent Statement: Not applicable.

Data Availability Statement: The original contributions presented in the study are included in the article, and further inquiries can be directed to the corresponding authors.

Acknowledgments: The authors extend their gratitude to Bor Cutting Tools Machine Industry Trade Ltd. Co. for their assistance in the processing of the parts used in this study and for providing technical support. The authors would also like to thank the Scientific Research Projects Coordination Unit of Istanbul Yeni Yuzyil University for supporting this publication.

Conflicts of Interest: The authors declare that they have no known competing financial interests or personal relationships that could have appeared to influence the work reported in this paper.

References

1. Solanke, S.; Gaval, V.; Sanghavi, S. In vitro tribological investigation and osseointegration assessment for metallic orthopedic bioimplant materials. *Mater. Today Proc.* **2021**, *44*, 4173–4178. [CrossRef]
2. Hagen, C.M.H.; Hognestad, A.; Knudsen, O.; Sørby, K. The effect of surface roughness on corrosion resistance of machined and epoxy coated steel. *Prog. Org. Coat.* **2019**, *130*, 17–23. [CrossRef]
3. Posner, R.; Ozcan, O.; Grundmeier, G. Water and Ions at Polymer/Metal Interfaces. In *Design of Adhesive Joints Under Humid Conditions. Advanced Structured Materials*; Springer: Berlin/Heidelberg, Germany, 2013; pp. 21–52. [CrossRef]
4. Kaur, M.; Singh, K. Review on titanium and titanium based alloys as biomaterials for orthopaedic applications. *Mater. Sci. Eng. C Mater. Biol. Appl.* **2019**, *102*, 844–862. [CrossRef] [PubMed]
5. Nicholson, J.W. Titanium Alloys for Dental Implants: A Review. *Prosthesis* **2020**, *2*, 100–116. [CrossRef]
6. Karabulut, G.; Üllen, N.B.; Karakuş, S.; Ersoy, M. Comparison of surface modification and corrosion resistance of Ti6Al4V alloy using matcha tea extract-based silver and copper oxide nanoparticles. *Surf. Coat. Technol.* **2024**, *480*, 130564. [CrossRef]
7. Alcudia, A.; Begines, B.; Rodriguez-Lejarraga, P.; Greyer, V.; Godinho, V.C.F.; Pajuelo, E.; Torres, Y. Development of porous silver nanoparticle/polycaprolactone/polyvinyl alcohol coatings for prophylaxis in titanium interconnected samples for dental implants. *Colloid Interface Sci. Commun.* **2022**, *48*, 100621. [CrossRef]
8. Alba-Cabañas, J.; Speranza, R.; Pedico, A.; Lamberti, A.; Vaillant-Roca, L. Enhancing coating uniformity and performance with zinc oxide nanoparticles interface layer in dye-sensitized cells. *Mater. Sci. Eng. B* **2024**, *310*, 117748. [CrossRef]
9. Jamkhande, P.G.; Ghule, N.W.; Bamer, A.H.; Kalaskar, M.G. Metal nanoparticles synthesis: An overview on methods of preparation, advantages and disadvantages, and applications. *J. Drug Deliv. Sci. Technol.* **2019**, *53*, 101174. [CrossRef]
10. Karabulut, G.; Üllen, N.B.; Karakuş, S.; Toruntay, C. Enhancing antibacterial and anticorrosive properties of 316L stainless steel with nanocoating of copper oxide nanoparticles. *Mater. Chem. Phys.* **2023**, *308*, 128265. [CrossRef]
11. Hamad, Q.A.; Faheed, N.K.; Issa, R.A.H. Wettability; morphological, miscibility characterization of alginate, and chitosan-based bio composite coatings. *Surf. Eng.* **2024**, *40*, 629–647. [CrossRef]
12. Karabulut, G.; Üllen, N.B.; Akyüz, E.; Karakuş, S. Surface modification of 316L stainless steel with multifunctional locust gum/polyethylene glycol-silver nanoparticles using different coating methods. *Prog. Org. Coat.* **2023**, *174*, 107291. [CrossRef]

13. Zhang, S.; Liang, X.; Gadd, G.M.; Zhao, Q. A sol–gel based silver nanoparticle/polytetrafluorethylene (AgNP/PTFE) coating with enhanced antibacterial and anti-corrosive properties. *Appl. Surf. Sci.* **2021**, *535*, 147675. [CrossRef]
14. Tavakoli, S.; Nemati, S.; Kharaziha, M.; Akbari-Alavijeh, S. Embedding CuO Nanoparticles in PDMS-SiO_2 Coating to Improve Antibacterial Characteristic and Corrosion Resistance. *Colloid Interface Sci. Commun.* **2019**, *28*, 20–28. [CrossRef]
15. Ferraris, S.; Spriano, S.; Pan, G.; Venturello, A.; Bianchi, C.L.; Chiesa, R.; Faga, M.G.; Maina, G.; Vernè, E. Surface modification of Ti–6Al–4V alloy for biomineralization and specific biological response: Part I, inorganic modification. *J. Mater. Sci. Mater. Med.* **2011**, *22*, 533–545. [CrossRef] [PubMed]
16. Roldán, M.V.; Castro, Y.; Pellegri, N.; Durán, A. Enhanced photocatalytic activity of mesoporous SiO_2/TiO_2 sol–gel coatings doped with Ag nanoparticles. *J. Sol-Gel Sci. Technol.* **2015**, *76*, 180–194. [CrossRef]
17. Sadanandan, B.; Krishna, P.M.; Kumari, M.; Vijayalakshmi, V.; Nagabhushana, B.M.; Vangala, S.; Singh, H.K.; Swaroopa, B.R.D.; Megala, V. Zinc oxide nanoparticles exhibit anti-cancer activity against human cell lines. *J. Mol. Struct.* **2024**, *1305*, 137723. [CrossRef]
18. Al-darwesh, M.Y.; Ibrahim, S.S.; Mohammed, M.A. A Review on Plant Extract Mediated Green Synthesis of Zinc oxide Nanoparticles and Their biomedical Applications. *Results Chem.* **2024**, *7*, 101368. [CrossRef]
19. Zeghoud, S.; Hemmami, H.; Seghir, B.B.; Amor, I.B.; Kouadri, I.; Rebiai, A.; Messaoudi, M.; Ahmed, S.; Pohl, P.; Simal-Gandara, J. A review on biogenic green synthesis of ZnO nanoparticles by plant biomass and their applications. *Mater. Today Commun.* **2022**, *33*, 104747. [CrossRef]
20. Naveenkumar, S.; Kamaraj, C.; Prem, P.; Raja, R.K.; Priyadharsan, A.; Alrefaei, A.F.; Govindarajan, R.K.; Thamarai, R.; Subramaniyan, V. Eco-friendly synthesis of palladium nanoparticles using Zaleya decandra: Assessing mosquito larvicidal activity, zebrafish embryo developmental toxicity, and impacts on freshwater sludge worm *Tubifex tubifex*. *J. Environ. Chem. Eng.* **2024**, *12*, 111912. [CrossRef]
21. Shao, X.; Wu, X.; Liu, H.; Wang, P.; Du, C.F.; Wang, L.; Wang, H.; Yang, J. Effect of nano-particles ZnO and layered GO on high temperature tribological performance of MoS_2-based heterojunction composite lubricating coating. *J. Mater. Sci.* **2024**, *59*, 19855–19874. [CrossRef]
22. Pandey, R.K.; Choi, H.; Yi, J.; Heo, J.; Sahu, P.K. Facile controlled synthesis of bifunctional ZnO nanoparticles for application as a high-performance self-powered UV photosensor and highly selective vapor sensor. *Mater. Sci. Eng. B* **2023**, *293*, 116470. [CrossRef]
23. Rafee, V.; Razaghizadeh, A.; Nakhaei, R.; Hosini, R. Eco-friendly dye-sensitized solar cells: Green synthesis of ZnO nanoparticles using Sargassum algae and performance enhancement through optimized dye combinations. *Mater. Sci. Eng. B* **2025**, *317*, 118164. [CrossRef]
24. Sedefoglu, N.; Veryer, K.; Zalaoglu, D.; Bozok, F. Antibacterial and photocatalytic performances of bioactive In-doped ZnO nanoparticles. *Mater. Sci. Eng. B* **2025**, *313*, 117914. [CrossRef]
25. Kumar, S.P.L.; Avinash, D. Review on effect of Ti-alloy processing techniques on surface-integrity for biomedical application. *Mater. Manuf. Process.* **2020**, *35*, 869–892. [CrossRef]
26. Singh, S.; Bala, N.; Kaur, A. Thermal spray coatings: For industrial and biomedical applications. *Surf. Eng.* **2026**, *42*, 486–506. [CrossRef]
27. Wu, L.K.; Wu, J.J.; Wu, W.Y.; Cao, F.H.; Jiang, M.Y. Sol–gel-based coatings for oxidation protection of TiAl alloys. *J. Mater. Sci.* **2020**, *55*, 6330–6351. [CrossRef]
28. Assender, H.; Bliznyuk, V.; Porfyrakis, K. How Surface Topography Relates to Materials' Properties. *Science* **2002**, *297*, 973–976. [CrossRef] [PubMed]
29. Kim, M.K.; Chung, D.D.L. Inductance-based sensing of surface roughness, with application to wear sensing. *J. Mater. Sci.* **2024**, *59*, 15816–15829. [CrossRef]
30. Paknahad, H.; Nogorani, F.S. Effects of substrate roughness on the surface morphology and corrosion properties of Fe- and Ni-aluminide coatings on martensitic stainless steel. *Surf. Coat. Technol.* **2020**, *392*, 125761. [CrossRef]
31. Alla, R.K.; Ginjupalli, K.; Upadhya, N.; Shammas, M.; Ravi, R.K.; Sekhar, R. Surface roughness of implants: A review. *Trends Biomater. Artif. Organs* **2011**, *25*, 112–118.
32. Mozammel, M.; Khajeh, M.; Ilkhechi, N.N. Effect of Surface Roughness of 316 L Stainless Steel Substrate on the Morphological and Super-Hydrophobic Property of TiO2 Thin Films Coatings. *Silicon* **2018**, *10*, 2603–2607. [CrossRef]
33. Sigma-Aldrich. Xanthan gum from *Xanthomonas campestris* (CAS No. 11138-66-2). Available online: https://www.sigmaaldrich.com/JP/ja/product/sigma/43708?srsltid=AfmBOooISU7AoTd1Ne-ApFqGBm6aP8PDQksi-TPJNWTIZNqGJAaEmgJh (accessed on 10 June 2026).
34. Pace, V.; Sinisterra, J.V.; Alcantara, A.R. Celite-Supported Reagents in Organic Synthesis: An Overview. *Curr. Org. Chem.* **2010**, *14*, 2384–2408. [CrossRef]
35. Altınsoy, Ş.; Üllen, N.B.; Ersoy, M.; Can, D. Machining Performance of Uncoated and Carbide Coated Cutting Inserts in Ti6Al4V Turning: An Experimental and Numerical Approach. *J. Mater. Eng. Perform.* **2024**, *34*, 4458–4476. [CrossRef]

36. Pramanik, A.; Littlefair, G. Machining of Titanium Alloy (Ti-6Al-4V)—Theory to Application. *Mach. Sci. Technol.* **2015**, *19*, 1–49. [CrossRef]
37. Cwickel, D.; Paz, Y.; Marmur, A. Contact angle measurement on rough surfaces: The missing link. *Surf. Innov.* **2017**, *5*, 190–193. [CrossRef]
38. Kubiak, K.J.; Wilson, M.C.T.; Mathia, T.G.; Carval, P. Wettability versus roughness of engineering surfaces. *Wear* **2011**, *271*, 523–528. [CrossRef]
39. Söz, C.K.; Yilgör, E.; Yilgör, I. Influence of the average surface roughness on the formation of superhydrophobic polymer surfaces through spin-coating with hydrophobic fumed silica. *Polymer* **2015**, *62*, 118–128. [CrossRef]
40. Zha, X.; Qin, H.; Yuan, Z.; Xi, L.; Zhang, T.; Jiang, F. Effect of cutting feed rate on machining performance and surface integrity in cutting process of Ti-6Al-4V alloy. *Int. J. Adv. Manuf. Technol.* **2023**, *131*, 2791–2809. [CrossRef]
41. Chelaru, J.D.; Muresan, L.M. Mercapto-5-acetylamino-1,3,4-thiadiazole as corrosion inhibitor for a naturally patinated monumental bronze artifact. *Stud. Univ. Babeș-Bolyai Chem.* **2014**, *59*, 91–102.
42. Mousavi, S.M.; Behbudi, G.; Gholami, A.; Hashemi, S.A.; Nejad, Z.M.; Bahrani, S.; Chiang, W.H.; Wei, L.C.; Omidifar, N. Shape-controlled synthesis of zinc nanostructures mediating macromolecules for biomedical applications. *Biomater. Res.* **2022**, *26*, 4. [CrossRef] [PubMed]
43. Lee, S.; Jeong, S.; Kim, D.; Hwang, S.; Jeon, M.; Moon, J. ZnO nanoparticles with controlled shapes and sizes prepared using a simple polyol synthesis. *Superlattices Microstruct.* **2008**, *43*, 330–339. [CrossRef]
44. Üllen, N.B.; Şevk, G.K.; Özarslan, A.C.; Kuçak, M. Surface integrity-dependent nanoparticle coating efficiency: Exploring sonochemically synthesized Zingiber officinale extract-based ZnO nanoparticles on Ti6Al4V. *J. Mater. Sci.* **2025**, *60*, 16328–16350. [CrossRef]
45. Ahmad, H.; Markina, A.A.; Porotnikov, M.V.; Ahmad, F. A review of carbon fiber materials in automotive industry. *IOP Conf. Ser. Mater. Sci. Eng.* **2020**, *971*, 032011. [CrossRef]
46. Karakus, S.; Tan, E.; Ilgar, M.; Sahin, Y.M.; Mansuroglu, D.S.; Ismik, D.; Somroo, R.A.; Kilislioglu, A. Swelling behaviour, rheological property and drug release profile of the anti-inflammatory drug metamizole sodium from xanthan gum–ZnO nanoparticles. *Polym. Bull.* **2022**, *79*, 357–380. [CrossRef]
47. Srivastava, V.; Gusain, D.; Sharma, Y.C. Synthesis, characterization and application of zinc oxide nanoparticles (n-ZnO). *Ceram. Int.* **2013**, *39*, 9803–9808. [CrossRef]
48. Mahalakshmi, S.; Hema, N.; Vijaya, P.P. In Vitro Biocompatibility and Antimicrobial activities of Zinc Oxide Nanoparticles (ZnO NPs) Prepared by Chemical and Green Synthetic Route—A Comparative Study. *Bionanoscience* **2020**, *10*, 112–121. [CrossRef]
49. Kalpana, V.N.; Rajeswari, V.D. A Review on Green Synthesis, Biomedical Applications, and Toxicity Studies of ZnO NPs. *Bioinorg. Chem. Appl.* **2018**, *2018*, 3569758. [CrossRef] [PubMed]
50. Sangeetha, G.; Rajeshwari, S.; Venckatesh, R. Green synthesis of zinc oxide nanoparticles by aloe barbadensis miller leaf extract: Structure and optical properties. *Mater. Res. Bull.* **2011**, *46*, 2560–2566. [CrossRef]
51. Kundu, D.; Hazra, C.; Chatterjee, A.; Chaudhari, A.; Mishra, S. Extracellular biosynthesis of zinc oxide nanoparticles using Rhodococcus pyridinivorans NT2: Multifunctional textile finishing, biosafety evaluation and in vitro drug delivery in colon carcinoma. *J. Photochem. Photobiol. B* **2014**, *140*, 194–204. [CrossRef] [PubMed]
52. Qian, Y.; Yao, J.; Russel, M.; Chen, K.; Wang, X. Characterization of green synthesized nano-formulation (ZnO–A. vera) and their antibacterial activity against pathogens. *Environ. Toxicol. Pharmacol.* **2015**, *39*, 736–746. [CrossRef] [PubMed]
53. Ali, K.; Dwivedi, S.; Azam, A.; Saquib, Q.; Al-Said, M.S.; Alkhedhairy, A.A.; Musarrat, J. Aloe vera extract functionalized zinc oxide nanoparticles as nanoantibiotics against multi-drug resistant clinical bacterial isolates. *J. Colloid Interface Sci.* **2016**, *472*, 145–156. [CrossRef] [PubMed]
54. Rasouli, R.; Barhoum, A.; Uludag, H. A review of nanostructured surfaces and materials for dental implants: Surface coating, patterning and functionalization for improved performance. *Biomater. Sci.* **2018**, *6*, 1312–1338. [CrossRef] [PubMed]
55. Wang, J.; Wu, Y.; Cao, Y.; Li, G.; Liao, Y. Influence of surface roughness on contact angle hysteresis and spreading work. *Colloid Polym. Sci.* **2020**, *298*, 1107–1112. [CrossRef]
56. Croll, S.G. Surface roughness profile and its effect on coating adhesion and corrosion protection: A review. *Prog. Org. Coat.* **2020**, *148*, 105847. [CrossRef]
57. Wen, G.; Guo, Z.; Liu, W. Biomimetic polymeric superhydrophobic surfaces and nanostructures: From fabrication to applications. *Nanoscale* **2017**, *9*, 3338–3366. [CrossRef] [PubMed]
58. Singhatanadgit, W. Biological Responses to New Advanced Surface Modifications of Endosseous Medical Implants. *Bone Tissue Regen. Insights* **2009**, *2*, BTRI.S3150. [CrossRef]
59. Bathomarco, R.V.; Solorzano, G.; Elias, C.N.; Prioli, R. Atomic force microscopy analysis of different surface treatments of Ti dental implant surfaces. *Appl. Surf. Sci.* **2004**, *233*, 29–34. [CrossRef]
60. Kilpadi, D.V.; Weimer, J.J.; Lemons, J.E. Effect of passivation and dry heat-sterilization on surface energy and topography of unalloyed titanium implants. *Colloids Surf. A Physicochem. Eng. Asp.* **1998**, *135*, 89–101. [CrossRef]

61. Islam, M.S.; Tong, L.; Falzon, P.J. Influence of metal surface preparation on its surface profile, contact angle, surface energy and adhesion with glass fibre prepreg. *Int. J. Adhes. Adhes.* **2014**, *51*, 32–41. [CrossRef]
62. Bharathidasan, T.; Kumar, S.V.; Bobji, M.S.; Chakradhar, R.P.S.; Basu, B.J. Effect of wettability and surface roughness on ice-adhesion strength of hydrophilic, hydrophobic and superhydrophobic surfaces. *Appl. Surf. Sci.* **2014**, *314*, 241–250. [CrossRef]
63. Kietzig, A.M.; Hatzikiriakos, S.G.; Englezos, P. Patterned superhydrophobic metallic surfaces. *Langmuir* **2009**, *25*, 4821–4827. [CrossRef] [PubMed]
64. Üllen, N.B.; Karabulut, G.; Karakuş, S. Assessing the Surface Properties of Plant Extract-Based Silver Nanoparticle Coatings on 17–4 PH Stainless Steel Foams Using Artificial Intelligence-Supported RGB Analysis: A Comparative Study. *J. Mater. Eng. Perform.* **2023**, *32*, 10637–10654. [CrossRef]
65. Matos, G.R.M. Surface Roughness of Dental Implant and Osseointegration. *J. Maxillofac. Oral Surg.* **2021**, *20*, 1–4. [CrossRef] [PubMed]
66. Bandapalli, C.; Singh, K.K.; Sutaria, B.M.; Bhatt, D.V. Experimental investigation of machinability parameters in high-speed micro-end milling of titanium (grade-2). *Int. J. Adv. Manuf. Technol.* **2016**, *85*, 2139–2153. [CrossRef]
67. Sobieszczyk, S. Surface modifications of Ti and its alloys. *Adv. Mater. Sci.* **2010**, *10*, 29–42. [CrossRef]
68. Benardos, P.G.; Vosniakos, G.C. Predicting surface roughness in machining: A review. *Int. J. Mach. Tools Manuf.* **2003**, *43*, 833–844. [CrossRef]
69. Abdelnasser, A.S.; Barakat, A.; Elsanabary, S.; Nassef, A. Relative Performance of Coated Ceramic and CBN Inserts in Hard Turning of Ti6Al4V Alloy. *Port-Said Eng. Res. J.* **2020**, *24*, 114–121. [CrossRef]
70. Albrektsson, T.; Wennerberg, A. Oral implant surfaces: Part 1—Review focusing on topographic and chemical properties of different surfaces and in vivo responses to them. *Int. J. Prosthodont.* **2004**, *17*, 536–543. [PubMed]
71. Jiang, P.; Zhang, Y.; Hu, R.; Shi, B.; Zhang, L.; Huang, Q.; Yang, Y.; Tang, P.; Lin, C. Advanced surface engineering of titanium materials for biomedical applications: From static modification to dynamic responsive regulation. *Bioact. Mater.* **2023**, *27*, 15–57. [CrossRef] [PubMed]
72. Ball, M.; Grant, D.M.; Lo, W.J.; Scotchford, C.A. The effect of different surface morphology and roughness on osteoblast-like cells. *J. Biomed. Mater. Res. A* **2008**, *86A*, 637–647. [CrossRef] [PubMed]
73. Caio, F.; Moreau, C. Influence of Substrate Shape and Roughness on Coating Microstructure in Suspension Plasma Spray. *Coatings* **2019**, *9*, 746. [CrossRef]
74. Tan, J.; Shah, S.; Thomas, A.; Ou-Yang, H.D.; Liu, Y. The influence of size, shape and vessel geometry on nanoparticle distribution. *Microfluid. Nanofluidics* **2013**, *14*, 77–87. [CrossRef] [PubMed]
75. Capco, D.G.; Chen, Y. (Eds.) *Nanomaterial*; Springer: Berlin/Heidelberg, Germany, 2014; Volume 811. [CrossRef]
76. Bernard, B.; Bianchi, L.; Malié, A.; Joulia, A.; Rémy, B. Columnar suspension plasma sprayed coating microstructural control for thermal barrier coating application. *J. Eur. Ceram. Soc.* **2016**, *36*, 1081–1089. [CrossRef]
77. Gurzawska, K.; Svava, R.; Syberg, S.; Yihua, Y.; Haugshøj, K.B.; Damager, I.; Ulvskov, P.; Christensen, L.H.; Gotfredsen, K.; Jørgensen, N.R. Effect of nanocoating with rhamnogalacturonan-I on surface properties and osteoblasts response. *J. Biomed. Mater. Res. A* **2012**, *100A*, 654–664. [CrossRef] [PubMed]
78. Altlnsoy, Ş.; Erkan, S.; Üllen, N.B.; Ateş, S.C.; Evcil, N. Evaluation of surface properties of modified Ti6Al4V alloy with copper nanoparticles organic nanostructure for biomedical applications: Dependency on anticorrosive, antibacterial, and biocompatibility. *Corros. Rev.* **2025**, *43*, 361–380. [CrossRef]
79. Perumal, P.; Ramanathan, K.; Ganesan, L.; Subramanian, B.; Ganesh, V.; Stalin, B. Investigation of TiN coating uniformity and its corrosion behaviour using image process. *Mater. Res. Express* **2019**, *6*, 046411. [CrossRef]
80. Saidi, R.; Raeissi, K.; Ashrafizadeh, F.; Kharaziha, M. The effect of zinc oxide coating morphology on corrosion performance of Ti-6Al-4 V alloys. *J. Alloys Compd.* **2021**, *883*, 160771. [CrossRef]
81. Thakur, V.K.; Thakur, M.K.; Kessler, M.R. (Eds.) *Handbook of Composites from Renewable Materials, Functionalization*; Wiley: Hoboken, NJ, USA, 2017.
82. Wennerberg, A.; Albrektsson, T. Effects of titanium surface topography on bone integration: A systematic review. *Clin. Oral Implants Res.* **2009**, *20*, 172–184. [CrossRef] [PubMed]
83. Gao, C.; Li, C.; Wang, C.; Qin, Y.; Wang, Z.; Yang, F.; Liu, H.; Chang, F.; Wang, J. Advances in the induction of osteogenesis by zinc surface modification based on titanium alloy substrates for medical implants. *J. Alloys Compd.* **2017**, *726*, 1072–1084. [CrossRef]
84. Rajesh, Y.; Purkayastha, D.D.; Krishna, M.G. Seed layer mediated wettability and wettability transition of ZnO nano/micro-rod arrays. *J. Alloys Compd.* **2021**, *857*, 157617. [CrossRef]
85. Creus, J.; Mazille, H.; Idrissi, H. Porosity evaluation of protective coatings onto steel, through electrochemical techniques. *Surf. Coat. Technol.* **2000**, *130*, 224–232. [CrossRef]
86. Mulijani, S.; Rizky, G.; Wulanawati, A.; Handayani, A.W.; Asih, F.N. Synthesis of Zinc Oxide Nanoparticle as Corrosion Resistance of Steel Metal. *AIP Conf. Proc.* **2022**, *2638*, 020006. [CrossRef]

87. Wu, N.; Gao, H.; Wang, X.; Pei, X. Surface Modification of Titanium Implants by Metal Ions and Nanoparticles for Biomedical Application. *ACS Biomater. Sci. Eng.* **2023**, *9*, 2970–2990. [CrossRef] [PubMed]
88. Woźniak-Budych, M.J.; Staszak, M.; Staszak, K. A critical review of dental biomaterials with an emphasis on biocompatibility. *Dent. Med. Probl.* **2023**, *60*, 709–739. [CrossRef] [PubMed]
89. Kuang, J.; Ba, Z.; Li, Z.; Wang, Z.; Qiu, J. The study on corrosion resistance of superhydrophobic coatings on magnesium. *Appl. Surf. Sci.* **2020**, *501*, 144137. [CrossRef]
90. Trentin, A.; Samiee, R.; Pakseresht, A.H.; Duran, A.; Castro, Y.; Galusek, D. Influence of pre-treatments on adhesion, barrier and mechanical properties of epoxy coatings: A comparison between steel, AA7075 and AA2024. *Appl. Surf. Sci. Adv.* **2023**, *18*, 100479. [CrossRef]
91. Amiriafshar, M.; Rafieazad, M.; Duan, X.; Nasiri, A. Fabrication and Coating Adhesion Study of Superhydrophobic Stainless Steel Surfaces: The Effect of Substrate Surface Roughness. *Surf. Interfaces* **2020**, *20*, 100526. [CrossRef]
92. Zhang, X.; Wang, H.; Li, J.; He, X.; Hang, R.; Huang, X.; Tian, L.; Tang, B. Corrosion behavior of Zn-incorporated antibacterial TiO_2 porous coating on titanium. *Ceram. Int.* **2016**, *42*, 17095–17100. [CrossRef]

Disclaimer/Publisher's Note: The statements, opinions and data contained in all publications are solely those of the individual author(s) and contributor(s) and not of MDPI and/or the editor(s). MDPI and/or the editor(s) disclaim responsibility for any injury to people or property resulting from any ideas, methods, instructions or products referred to in the content.